

Mixed-phase clouds and precipitation in Southern Ocean cyclones and cloud systems observed poleward of 64°S by ship-based cloud radar and lidar

S. P. Alexander^{1,2}, G. M. McFarquhar³, R. Marchand⁴, A. Protat^{5,2}, É. Vignon^{6,7}, G. G. Mace⁸, A. R. Klekociuk^{1,2}

¹Australian Antarctic Division, Kingston, Tasmania, Australia

²Australian Antarctic Program Partnership, Institute for Marine and Antarctic Studies, University of Tasmania, Hobart, Tasmania, Australia

³Cooperative Institute for Mesoscale Meteorological Studies and the School of Meteorology, University of Oklahoma, Norman, OK, USA

⁴Department of Atmospheric Sciences, University of Washington, Seattle, WA, USA

⁵Bureau of Meteorology, Melbourne, Australia

⁶Environmental Remote Sensing Laboratory (LTE), École Polytechnique Fédérale de Lausanne (EPFL), Lausanne, Switzerland

⁷Laboratoire de Météorologie Dynamique IPSL, Sorbone Universités, CNRS, Paris, France

⁸Department of Atmospheric Sciences, University of Utah, Salt Lake City, UT, USA

Key Points:

- Generating cells at the top of mid-level mixed-phase clouds are commonly observed over the high-latitude Southern Ocean
- Supercooled drizzle is present in two of the three cases examined here with phase changes following supercooled liquid layer seeding
- Seeding of single-layer ice-precipitating supercooled liquid clouds occurs in the trailing clouds of each system

Corresponding author: Simon Alexander, simon.alexander@aad.gov.au

This article has been accepted for publication and undergone full peer review but has not been through the copyediting, typesetting, pagination and proofreading process, which may lead to differences between this version and the [Version of Record](#). Please cite this article as [doi: 10.1029/2020JD033626](https://doi.org/10.1029/2020JD033626).

This article is protected by copyright. All rights reserved.

Abstract

Mixed-phase clouds (MPCs), composed of both liquid and ice, are prevalent in Southern Ocean cyclones. A characterisation of these clouds on fine vertical scales is required in order to understand the microphysical processes within these clouds, and for model and satellite evaluations over this region. We investigated three examples of cloud systems collected by ship-mounted remote sensing instruments adjacent to East Antarctica at latitudes between 64°S and 69°S. These cases allow us to examine the properties of mid-level MPCs, with cloud tops between 2 and 6 km. Mid-level MPCs contain multiple layers of supercooled liquid water (SLW) embedded within ice during the passage of cyclones. SLW layers are capped by strong temperature inversions and are observed at temperatures as low as -31°C . Convective generating cells (GCs) are present inside supercooled liquid-topped mid-level MPCs. The horizontal extent, vertical extent and maximum upward Doppler velocity of these GCs were 0.6 – 3.6 km, 0.7 – 1.0 km and 0.5 – 1.0 m s^{-1} , respectively, and are consistent with observations from previous lower-latitude studies. Ice precipitation is nearly ubiquitous, except in the thinnest clouds at the trailing end of the observed systems. Seeding of lower SLW layers from above leads to periods with either larger ice particles or greater ice precipitation rates. Periods of supercooled drizzle lasting up to two hours were observed toward the end of two of the three cyclone systems. This supercooled drizzle turns into predominantly ice precipitation as the result of seeding by ice clouds located above the precipitating SLW layer.

1 Introduction

Mixed-phase clouds (MPCs) containing both ice and liquid occur commonly from the tropics to the polar regions (e. g. Hogan et al. (2003); McFarquhar et al. (2007); Hu et al. (2010); Mioche, Jourdan, Ceccaldi, and Delanoë (2015)). These clouds remain difficult to model correctly due to the interplay of microphysical and dynamical processes which regulate their formation, maintenance and decay (Sotiropoulou et al., 2016), and because the scales over which these processes occur are substantially smaller than the resolution of climate and weather prediction models. The observed longevity of MPCs indicates that the removal of ice crystals from the cloud through gravitational sedimentation must be balanced by a continuous source of liquid water. Intra-cloud processes including updrafts and turbulent mixing, or a continuous supply of new liquid at cloud base, must be sufficient to replenish the liquid water (Rauber & Tokay, 1991; Korolov

56 & Field, 2008). The correct modelling of cloud phase partitioning between ice and liq-
57 uid water is necessary to match observations of reflected shortwave radiation (Forbes &
58 Ahlgrim, 2014; Kay et al., 2016; Tan et al., 2016; Lenaerts et al., 2017). Cloud phase
59 was recently shown to strongly influence Antarctic ice shelf surface melting (Gilbert et
60 al., 2020). The presence of multi-layered MPCs reported in the extra-tropics indicates
61 that these clouds can exist and persist in a complex environment (Verlinde et al., 2013).
62 Initiation of upper (or free-tropospheric) MPC layers are often due to large scale advec-
63 tion of moisture, while MPC layers closer to the surface are also influenced by surface
64 processes such as heat and moisture fluxes and turbulence. (Luo et al., 2008)

65 The upper part of an idealized mid-level MPC (which we refer to here as being those
66 clouds with tops between 2 km and 6 km altitude and temperatures between -10°C and
67 -30°C) often consists of a thin supercooled liquid water (SLW) layer of thickness less
68 than about 300 m (Hogan et al., 2003; Ansmann et al., 2009; Barrett et al., 2020), be-
69 neath which supercooled drizzle and/or ice precipitation may be present. The depth of
70 this precipitating layer depends upon the depth of ice supersaturation but is usually much
71 greater than the thickness of the SLW layer itself (Rauber & Tokay, 1991). The liquid
72 nature of these cloud tops results in strong radiative cooling by reflecting incoming short-
73 wave radiation and emitting longwave radiation (Heymsfield et al., 1991; Hogan et al.,
74 2003). The longwave emission produces strong cooling at cloud top that initiates tur-
75 bulent mixing driven by the negatively buoyant air parcels and a large temperature in-
76 version is observed at cloud top height due to this turbulent mixing and radiative cool-
77 ing. Ice particles are formed inside the liquid layer through heterogeneous freezing and
78 secondary ice production processes and grow rapidly by vapor deposition, riming and
79 aggregation. Another temperature inversion may be evident at the base of the ice virga
80 layer due to latent cooling as the ice particles sublimate in a drier air mass (Forbes &
81 Hogan, 2006). It remains unclear whether this idealized description is applicable to MPCs
82 found over the Southern Ocean and coastal Antarctica due to a lack of observational data.

83 MPCs are present throughout the lifecycle of extra-tropical cyclones, both within
84 ice clouds (of several kilometers vertical extent) and in post-frontal boundary-layer clouds
85 (Field et al., 2004; Jackson et al., 2012; Noh et al., 2019). Generating cells (GCs) and
86 their associated fall streaks occur frequently within extra-tropical cyclones and are im-
87 portant for understanding surface precipitation due to their role in ice production (Kumjian
88 et al., 2014; Cunningham & Yuter, 2014; Plummer et al., 2015; Keppas et al., 2018). These

89 GCs are small regions of convection located at or near cloud top, and exhibit relatively
90 large updraft speeds (of the order of $1 - 2 \text{ m s}^{-1}$), and a confined vertical and horizon-
91 tal extent ($1 - 2 \text{ km}$ and less than a few kilometers, respectively) (Rosenow et al., 2014).
92 These GC characteristics are consistent between cyclones, but on the other hand the tem-
93 perature and altitude at which GCs occur can vary markedly (Kumjian et al., 2014). Air-
94 craft observations of generating cells over the Southern Ocean (between 43°S and 61°S)
95 revealed a mean horizontal scale of around 400 m (Y. Wang et al., 2020), which is lower
96 than mean Northern Hemisphere GC scales.

97 Satellite and surface-based observations suggest that SLW clouds and low-altitude
98 SLW-topped MPCs are particularly common in the Southern Ocean compared to other
99 regions of the world (Ceppi et al., 2016; Choi et al., 2014; Marchand et al., 2009; Storelvmo
100 et al., 2015; Hu et al., 2010; Kanitz et al., 2011; A. E. Morrison et al., 2011; Huang et
101 al., 2012), and are likely more common than above oceans in the Northern Hemisphere
102 at similar latitudes (Ceppi et al., 2016; Choi et al., 2014; Huang et al., 2014; McCoy et
103 al., 2014). This may be due to the relatively low ice nucleating particle (INP) concen-
104 tration in this region (Burrows et al., 2013; McCluskey et al., 2018), which inhibits pri-
105 mary ice production within the clouds and could restrict precipitation. The ubiquity of
106 low-level cloud over the Southern Ocean (Haynes et al., 2011; Marchand et al., 2009) makes
107 understanding boundary layer cloud processes and microphysics from space challenging,
108 because satellite-based products suffer from phase uncertainty beneath cloud top height,
109 especially in the presence of multiple cloud decks (Mace, 2010). Surface-based remote-
110 sensing and in-situ observations are therefore required to quantify cloud properties and
111 complement the satellite observations (Listowski et al., 2019). Recent campaigns have
112 begun to address the paucity of these data over the Southern Ocean by employing air-
113 craft (Chubb et al., 2013; Huang et al., 2015) and ship-based platforms (Protat et al.,
114 2017; Mace & Protat, 2018a; Alexander & Protat, 2019; Kuma et al., 2020; Klekociuk
115 et al., 2020) to quantify cloud, aerosol, and precipitation properties, and evaluate mod-
116 els and satellite retrievals.

117 Although characterisation of MPCs in the Arctic using surface-based active remote
118 sensors is further advanced than at high Southern latitudes (e. g. H. Morrison et al. (2012);
119 Verlinde et al. (2013)), it is unlikely that the results from the Arctic are translatable to
120 the Southern Ocean and coastal Antarctic region due to differences in aerosol concen-
121 trations, meteorology and surface forcing. The Southern Ocean is characterised by strong

122 surface winds and the continuous passage of extratropical cyclones and associated frontal
123 cloud systems throughout the year. The winds experienced along and adjacent to much
124 of coastal East Antarctica are a mixture of local katabatic forcing from the interior of
125 the continent, and intermittent strong north-easterly winds associated with the passage
126 of warm fronts from the cyclones centred in the storm track further north (Turner et al.,
127 2009; Orr et al., 2014; Alexander et al., 2017). Correct cloud phase representation is also
128 necessary for correctly modelling snow melting along the Antarctic coastline (King et
129 al., 2015; Gilbert et al., 2020).

130 In this study, we examine aspects of clouds and precipitation in three extra-tropical
131 systems which were located close to the East Antarctic coastline. The clouds in the warm
132 and cold sectors of two cyclone passages are examined for two of these cases, while the
133 third case is an example of an extensive cloud system formed in the presence of a weak
134 trough. We use observations collected by a suite of instruments deployed aboard an ice-
135 breaking ship during the Measurements of Aerosols, Radiation and Clouds over the South-
136 ern Oceans (MARCUS) campaign to determine characteristics of generating cells, mixed-
137 phase cloud occurrence, and precipitation phase. Such characterisation, and the iden-
138 tification of the synoptic-scale forcings and the thermodynamic environment in which
139 MPCs exist, is necessary if we are to understand their presence, prevalence, evolution
140 and endurance over this near-coastal region. Section 2 describes the data used. We ex-
141 amine the three systems in detail in Section 3, including their generating cells and pre-
142 cipitation phase. The results are then discussed and related to prior observations in Sec-
143 tion 4 before the conclusions in Section 5.

144 **2 Data and analysis**

145 The MARCUS project installed instruments from the DoE Atmospheric Radiation
146 Measurements (ARM) Mobile Facility 2 (AMF2) aboard the Australian icebreaking ves-
147 sel *RSV Aurora Australis* between November 2017 and March 2018 (McFarquhar et al.,
148 2021). A comprehensive suite of instrumentation collected data during three transits be-
149 tween Australia and Antarctica, and one between Australia and Macquarie Island, dur-
150 ing the summer season. The MARCUS instrumentation used in the present study are
151 summarised in Table 1.

152 All data analysed in this study were acquired during the third *RSV Aurora Aus-*
153 *tralis* voyage (V3) of the summer season. MWACR data are calibrated by adding 4.5 dB
154 to the reflectivity profiles provided by ARM. This value was deduced from evaluations
155 of the MARCUS MWACR reflectivity against the calibrated W-band cloud radar on-
156 board the CAPRICORN-II voyage over similar latitudes and times (Mace et al., 2021),
157 and is consistent with the ARM cloud radar offsets identified by Kollias, Treserras, and
158 Protat (2019). The MWACR was mounted on a stabilizing platform which helped en-
159 sure that it remained vertically pointing, although as we will detail below, the ship’s heave,
160 pitch and roll during the three case studies was minimal.

161 Raw 532 nm backscatter return signals from the MPL are processed to remove back-
162 ground noise, corrected for beam overlap, and are then calibrated using lidar signal from
163 aerosol-free regions above the boundary layer, following Alexander and Protat (2018).
164 Cloud base and vertical extent (up to the limit of lidar signal attenuation) are calculated
165 from the calibrated backscatter and depolarisation ratio profiles following the return sig-
166 nal gradient algorithm described in Z. Wang and Sassen (2001). Uncertainty in cloud
167 base height is due to the inherently noisy nature of the backscatter gradients, which is
168 reduced by vertically smoothing the backscatter profiles with a five-point smoothing func-
169 tion. This smoothing is performed prior to determining the maximum gradient in backscat-
170 ter, which we assign to be the cloud base height. Cloud phase is determined using the
171 results from Hu et al. (2010), including accounting for horizontally-oriented ice plates
172 because the MPL points vertically. We firstly determine cloud base height, vertical ex-
173 tent and phase of those clouds which exceed a large backscatter gradient threshold at
174 cloud base (note that there is little sensitivity to the actual threshold value set). These
175 clouds are predominantly, but not exclusively, liquid water. We then separately calcu-
176 late cloud base height, vertical extent and phase of clouds which have small backscat-
177 ter gradients at cloud base. This method successfully identifies multiple SLW layers em-
178 bedded in MPCs, which are often visible in the raw lidar data over the high latitude South-
179 ern Ocean. The inferred cloud top height may be lower than the true cloud-top due to
180 lidar signal attenuation, but (as we will find later) the total amount of liquid water and
181 attenuation is often small in these mid-level MPCs in the absence of precipitation.

182 We perform a Monte Carlo simulation using a random population of $N = 1000$
183 samples from a normally-distributed population in order to quantify the uncertainty of
184 attributing the cloud phase (e. g. Alexander, Klekociuk, McDonald, and Pitts (2013)).

185 For each integrated cloud attenuated backscatter β_{int} and integrated depolarisation ratio
186 δ_{int} point, we have an associated uncertainties $\Delta\beta_{int}$ and $\Delta\delta_{int}$, which we set to be
187 twice the standard deviation of the normal distribution. We then determine the cloud
188 phase for each of these 1000 realisations. These simulations indicate that we misclassify
189 around 1% of the SLW as ice across the total of eight days of lidar observations used in
190 these three case studies.

191 We also use data from the 1290-MHz Beam-Steered Radar Wind Profiler (BSRWP)
192 in order to characterise the horizontal wind field. These data are available at one-hour
193 temporal resolution and at a maximum altitude of 5 km, although data gaps in the up-
194 per altitudes are not uncommon. Radiosondes were launched every six hours from the
195 ship for the entire summer campaign, providing a unique and valuable upper-air dataset
196 over the Southern Ocean and sea-ice zone (Sato et al., 2018). The radiosonde data are
197 used for investigating the detailed thermodynamics during SLW and virga cases. Data
198 from a two-channel microwave radiometer (MWR) are used to calculate liquid water path
199 (LWP) and precipitable water vapor (PWV) (Marchand et al., 2003). ERA5 (European
200 Centre for Medium-Range Weather Forecasting: Reanalysis Fifth Generation) (Hersbach
201 et al., 2020) thermodynamic data at the native resolution of $0.25^\circ \times 0.25^\circ$ from the nine
202 closest grid-cells to the ship's location are interpolated to provide the vertical temper-
203 ature profiles above the ship.

204 The primary objectives of V3 were to conduct the annual victualling resupply of
205 Mawson station (67.6°S , 62.9°E) and retrieve summer personnel at Davis station (68.6°S ,
206 78.0°E). We investigate three events when the ship was south of the oceanic polar front
207 and close to East Antarctica. The area of East Antarctica relevant for this study is shown
208 in Figure 1. The location of both stations, the ship's track into Davis and the locations
209 of the radiosonde launches made during the three case studies are indicated. The Febru-
210 ary 2018 mean sea ice concentration from ERA5 reveals remnant sea ice present offshore
211 from Mawson during this period. The sea conditions were calm during the sampling pe-
212 riods, with the small amounts of remnant first-year sea-ice acting to damp most ocean
213 swell. We discuss details of the ship's heave, roll and pitch in the case study analyses be-
214 low.

3 Results

3.1 Case 1: Voyage into Davis (64°S – 69°S) on 25 - 26 January 2018

3.1.1 Overview of event

The METOP-A satellite image of the regional cloud structure and the ERA-5 500 hPa geopotential height at 04 UT 26 January is shown in Figure 2, which is a time near the start of this case study. A ridge of high pressure extends southward from the mid-latitudes, with a weak shortwave trough to the west of the ship supporting extensive mid-level cloud cover above the ships track. This large-scale mid-level cloud system propagated eastwards over the course of the 26 January and was replaced by a homogeneous cloud layer with lower cloud tops above the ship's track (not shown). A cyclone is developing far to the west of Davis, upstream of this blocking ridge.

The cloud phase and background thermodynamic structure as observed by the MARCUS instruments onboard *RSV Aurora Australis* as the ship transited into Davis on 25 – 26 January 2018 are summarised in Figure 3. Solar midnight is around 19 UT at the longitude of Davis. Shallow low-level mixed-phase clouds are seen between 18 UT 25 January and 03 UT 26 January as the ship traversed latitudes 64°S – 65°S. These are typical of the duration, mixed-phase and vertical extent of boundary-layer clouds observed at lower latitudes over the Southern Ocean (Mace & Protat, 2018a; Noh et al., 2019). The hourly horizontal wind field from the BSRWP reveals a predominantly westerly flow up to the 5 km limit of wind detection. Deep precipitating ice clouds are evident between 06 UT and 14 UT 26 January. Liquid layers (if present) could not be detected during these times due to attenuation of the lidar signal. Surface temperatures do not exceed freezing throughout the event. Radar reflectivities are notably lower after 14 UT 26 January and multiple SLW layers embedded within ice become evident after 16 UT 26 January. Weakening southwesterly winds of less than 10 m s⁻¹ predominate inside these trailing clouds. Attenuation of the lidar signal by low clouds means that it is only sporadically possible to detect liquid in the upper layer (between 3 and 4 km), although it seems likely that a liquid layer persists throughout. Liquid water path decreases from 12 UT 26 January onwards as the radar reflectivity drops and cloud base height rises.

244

3.1.2 *Generating cells*

245

246

247

248

249

250

251

252

253

254

255

256

Figure 4 shows the period 17 – 18 UT 26 January and reveals the intricate structure of these clouds on fine temporal and spatial scales. Convective generating cells are present in the upper-level cloud region (2.3 – 3 km altitude) above the middle SLW layer. The MPL detects the 3 km cloud top prior to 1715 UT, before lower-level SLW layers become too optically thick. Ice is forming in the coldest, highest parts of the SLW layer, in this case at temperatures around -13°C . Ice fall streaks are readily visible in the MWACR reflectivity. Thickening of the lowest-level SLW layer inhibits identification of the SLW at upper levels after 1730 UT due to the near-full attenuation of the lidar signal. The uppermost SLW layer is present (where detectable by the MPL) inside and between GCs. This is consistent with aircraft observations which indicated minimal difference between liquid water content inside and between GCs over the open Southern Ocean (Y. Wang et al., 2020).

257

258

259

260

261

262

263

264

265

266

267

268

The temperature, relative humidity and wind speed and direction measured by a radiosonde launched at 1732 UT and passing through these multi-layered SLW and ice virga are shown in Figure 5. A well-mixed layer, capped by a 3°C temperature inversion at SLW cloud top height, is seen in the profile of the potential temperature θ between 2.6 km and 3.1 km altitude. This altitude corresponds to the convective generating cell region identified previously between the two uppermost SLW layers. Weak wind speeds of $< 5 \text{ m s}^{-1}$ are present inside the cloud at altitudes below about 2.3 km, but increase to 10 m s^{-1} at cloud top. Liquid layers near 1.5 and 2 km are associated with weak temperature inversions. The θ increases inside the ice virga (above 0.5 km altitude), consistent with warming of the environment by longwave absorption by precipitating ice. The lowest-level SLW layer is capping the boundary layer (compare with Figure 4) and may be coupled with the ocean surface.

269

270

271

272

273

274

275

We show the MWACR reflectivity between 1719 – 1737 UT 26 January in Figure 6a, with GCs clearly visible throughout the interval. The MWACR’s Doppler velocity (i. e. the sum of particle fall speed and vertical air motion) is displayed for this interval in Figure 6b. The ship’s speed over ground (seafloor) was 7 m s^{-1} , heading 175° and the pitch and roll were always $< 0.2^{\circ}$ during this time. We display the Doppler velocity profiles which have not been corrected for the ship’s heave because this is negligible. Specifically, during the time interval shown in Figure 6b, the root-mean-square (rms) of the heave

276 velocities (which were sampled at 10 Hz) was 0.07 m s^{-1} . Individual generating cells (GCs)
 277 occur in the upper part of the cloud, with a vertical extent of $0.7 - 0.8 \text{ km}$. Doppler ve-
 278 locities reach 1.0 m s^{-1} directly above the $2.5 - 2.6 \text{ km}$ SLW layer and are close to 0 m s^{-1}
 279 at cloud top altitude of 3.1 km . The Doppler spectra is shown in Figure 6c for data col-
 280 lection starting at 1728 UT and lasting 2 s, which is in the middle of a convective GC.
 281 A bimodal structure is evident around 2.3 km altitude, with a secondary peak in the spec-
 282 tra evident at 0 m s^{-1} . This is indicative of a population of SLW droplets and corresponds
 283 to the SLW layer as visible in the MPL data. A wavelet analysis on time-series of reflec-
 284 tivity within the GCs indicates that these predominantly had a duration of around 2 min-
 285 utes (not shown). Given the motion of the ship at this time, and the prevailing wind speed
 286 within the clouds of 5 m s^{-1} from 240° (from Figure 5), we estimate the horizontal ex-
 287 tent of these convective cells to be about 1.2 km .

288 *3.1.3 SLW layers and precipitation phase*

289 Figure 7 shows the last seven hours of this event. Three separate SLW layers are
 290 identifiable between 1.5 km and 3 km altitude after 1630 UT. There is an increasing dis-
 291 tance between the top two SLW layers, perhaps due to thermally induced circulations
 292 within the cloud driven by cloud top radiative cooling. The low volume depolarisation
 293 ratio δ_v below SLW cloud base indicates that supercooled drizzle is likely falling out of
 294 these clouds prior to 17 UT. This precipitation phase transitions to be predominantly
 295 ice after 1730 UT: the δ_v below SLW cloud base increases and the LWP decreases to val-
 296 ues close to zero which indicates insufficient liquid water for the precipitation to be driz-
 297 zle. After 2030 UT, ice precipitating out of the SLW layer above 3 km sublimates be-
 298 fore reaching the SLW layer located at $2 - 2.3 \text{ km}$ altitude.

299 The MWACR reflectivity is larger in the ice clouds below 2 km between 1730 UT
 300 and 1930 UT than before 1730 UT, which corresponds to the time when ice falling from
 301 the highest SLW layer intercepts the second SLW layer. This increase in reflectivity can
 302 either be due to an increase in ice particle size (through riming), or an increase in ice
 303 concentration. The increased reflectivity coincides with vertically continuous observa-
 304 tions of ice from the supercooled liquid cloud top at 3 km altitude down through all the
 305 SLW layers, i. e. seeding of the lowest boundary-layer coupled SLW cloud layer by ice
 306 produced in the generating cells at cloud top. Note that the MWACR reflectivity indi-
 307 cates the presence of some ice within the drizzle prior to 1730 UT.

3.2 Case 2: Passage of a cyclone above Mawson on 11 – 13 February 2018

The *RSV Aurora Australis* spent nearly two weeks at Mawson for the annual station resupply. During ‘daytime’ operating hours, the ship was moored in the harbour adjacent to the station. During local ‘night’ (solar midnight is around 20 UT), or during periods of inclement weather, the ship repositioned a few nautical miles offshore. This small variation in position is insignificant for our analysis of synoptic-scale cloud systems associated with two consecutive cyclones whose centers passed north of Mawson. Broken pack-ice was still present offshore of Mawson during these two weeks, with a coastal polynya keeping the near-shore region largely ice-free.

3.2.1 Overview of event

The first cyclone passage studied over Mawson occurred between 11 – 13 February 2018. Figure 8 shows the satellite image of the synoptic cloud field and 500 hPa geopotential height at 04 UT 13 February, which is a time toward the end of this event. The cyclone was centred around 64°S during these three days and weakened as it propagated from west of Mawson station to a position north of Davis by 04 UT 13 February. Earlier satellite images and ERA-5 thermodynamic fields reveal a warm front preceding the cyclone’s passage, while the cold front associated with this cyclone remained far to the north of the continent (not shown). The Patchy low and mid-level clouds are visible directly offshore of Mawson at 04 UT 13 February in Figure 8 in the cold sector of the cyclone, which will be discussed in detail below.

The radar reflectivity and thermodynamic profiles during the event are shown in Figure 9. Low-level wind below 1 km altitude is likely a mix of the synoptic-scale winds and an enhancement in the katabatic winds. Indeed, such wind structure observed at the East Antarctic continental margin is typically observed during the passage of offshore cyclones (Orr et al., 2014; Alexander et al., 2017). SLW layers observed by the lidar at 4 - 5 km altitude near the start of the event (14 - 16 UT 11 February), along with strong westerly winds, correspond to the warm conveyor belt and the warm front as identified along coastal East Antarctica (Jullien et al., 2020). Radar reflectivity decreases and cloud top height lowers after 12 UT 12 February with evidence of multiple SLW layers within the ice clouds. MODIS Aqua retrievals (MYD06) near 10 UT on 12 February indicate the cloud-top phase is liquid, with a total column optical depth between about 15 and

339 30 (not shown). The MARCUS MPL is heavily attenuated at this time, and is unable
340 to detect SLW at cloud top. While it would not be surprising (given the frequent pres-
341 ence of SLW near cloud top), it is ambiguous as to whether or not there is liquid water
342 at cloud-top at this time or whether MODIS is responding to the the liquid further down
343 in the cloud. A single-layer MPC persists in the light wind conditions at 2 km altitude
344 after 00 UT 13 February, consistent with MODIS Terra imagery that shows thin and some-
345 what patchy clouds near 05 UT on 13 February (not shown; MOD06 retrievals were largely
346 unsuccessful at this time). Note the presence of a thick ice cloud centred on 02 UT 13 Febru-
347 ary which is precipitating into the SLW. We will discuss this event in Section 3.2.3.

348 *3.2.2 Generating cells*

349 Convective GCs are present during Case 2: the radar reflectivity and Doppler ve-
350 locity between 1541 – 1559 UT 15 February are shown in Figure 10, along with the spec-
351 tra at 1544 UT. Upward motions reaching up to 1.0 m s^{-1} are present with 0.5 km of
352 cloud top. The temporal scale of these GCs calculated from a wavelet analysis (not shown)
353 varies between 2 –3 minutes. If we assume that the wind speed at cloud top height of
354 these GCs is 20 m s^{-1} (the value taken from the closest radiosonde profile, launched at
355 1732 UT 11 February), the spatial scale of these GCs is 2.4 – 3.6 km. The thick ice clouds
356 fully attenuated the lidar signal (not shown) thus we have no information on the pres-
357 ence or absence of SLW within these GCs, but microwave radiometer data indicates that
358 liquid water is present during this time.

359 *3.2.3 SLW layers and precipitation phase*

360 Figure 11 shows details of the clouds observed toward the end of the Case 2 cyclone.
361 Similar to the observations made of Case 1 (the transit into Davis), multiple layers of
362 SLW clouds are apparent, although it is difficult to identify the SLW layer at ice cloud
363 top before 18 UT 12 February due to opaque lower-level SLW layers. The SLW layer around
364 3 km altitude ascends in time and corresponds to a narrow vertical band with a decrease
365 in MWACR reflectivity (most clearly visible in Figure 11a directly after the 1800 UT SLW
366 layer, or directly before the 1930 UT SLW layer).

367 A layer of SLW with base around 2 km is identified throughout this part of the event.
368 The δ_v beneath this SLW layer (Figure 11c) indicate the presence of supercooled driz-

369 zle between 00 – 02 UT 13 February. The sudden increase in δ_v below the SLW layer af-
370 ter 02 UT 13 February indicates the dominance of precipitating ice, although we can-
371 not rule out the possibility of small amounts of supercooled drizzle also being present.
372 The liquid water path (Figure 11d) is large enough to support the existence of super-
373 cooled drizzle during this time. The observation of precipitating ice between 0200 - 0330 UT
374 matches the intersection of the 2 km altitude SLW layer by a high-level ice cloud (Fig-
375 ure 11a).

376 The two radiosonde profiles obtained during this interval (Figure 12) indicate an
377 inversion layer at cloud top height (an inversion of 3°C at 4 km at 1730 UT; and 4°C
378 at 2.5 km at 2332 UT). The θ profile below cloud top indicates a well-mixed region in-
379 side the MPC at 2332 UT. A shallow, well-mixed near surface layer due to the katabatic
380 wind is apparent at 2332 UT. The strong wind shear above the jet may be an intense
381 source of mixing.

382 **3.3 Case 3: Passage of the following cyclone above Mawson on 14 – 16 Febru-** 383 **ary 2018**

384 **3.3.1 Overview of event**

385 The following cyclone also passed north of Mawson and produced cloud bands vis-
386 ible above the ship from 14 – 16 February 2018. Mid-level ice seeding and a single SLW
387 layer precipitating ice at temperatures below -30°C will be described, but for this case
388 we find no evidence of supercooled drizzle, which is in contrast to the two prior case stud-
389 ies. The imminent arrival at Mawson of the cyclone’s warm front and associated cloud
390 bands are visible in the satellite cloud image and geopotential height data at 19 UT 14 Febru-
391 ary in Figure 13. The cold front associated with this cyclone, as with the previous Maw-
392 son cyclone, remained well to the north of the continent (not shown, see Vignon et al.
393 (2021) for further details). Satellite images and thermodynamic data from later times
394 indicate that this cyclone weakened as it propagated south-eastward toward the coast,
395 with cloud dissipating in a mid-level westerly flow on 16 January (not shown).

396 Boundary-layer mixed-phase clouds are present before 20 UT 14 February, preced-
397 ing the arrival of the warm front. A mixed-phase cloud (liquid water layer at 5.7 km pre-
398 cipitating ice virga) is present from 16 UT 14 February (Figure 14). These high-level SLW
399 clouds are commonly observed over the Southern Ocean (McFarquhar et al., 2021). This

400 mixed-phase cloud descends in time, maintaining cloud top temperatures of about -30°C .
401 Liquid water path (LWP) is much larger when shallow boundary-layer mixed-phase clouds
402 are observed than when only the mid-level SLW layer is present. The horizontal wind
403 field within the ice remains light (at least at altitudes below 5 km, which is the maxi-
404 mum range of the BSRWP). Similar to the previous case study, winds above 4 km alti-
405 tude veer from north-westerly to northeasterly and the temperature rises above 3 km
406 altitude as the cloud base height decreases. The winds and SLW clouds again indicate
407 the presence of a warm front, following the model of Keppas et al. (2018). Thick ice clouds
408 persist until around 06 UT 16 February, well after the surface pressure starts to rise. Sin-
409 gular layers of SLW cloud occur in regions of light wind from about 11 UT 16 February
410 onward.

411 *3.3.2 Generating cells*

412 The radar reflectivity, Doppler velocity and spectra of the GCs present between 1039
413 – 1057 UT 15 February are shown in Figure 15. The thick ice clouds fully attenuated
414 the lidar signal (not shown) thus we have no information on the presence or absence of
415 SLW within these GCs, but microwave radiometer data indicate the presence of liquid
416 water. The Doppler velocities are displayed without correction for the negligible heave
417 velocities during this time interval: the rms heave velocity during this time was 0.004 m s^{-1} .
418 The overall features of the GCs seen in this event are consistent with those reported in
419 Case 1 and Case 2. GCs have vertical extent around 0.9 km, fall streaks are clearly ev-
420 ident, and the wavelet spectra indicate dominant temporal scales of 1 minute and 3 min-
421 utes (not shown). Wind speeds at cloud top height were around 10 m s^{-1} (obtained from
422 the 1130 UT radiosonde profile, not shown), thus the spatial scale of these GCs varied
423 from 0.6 – 1.8 km during this interval. The Doppler velocity spectra at 1048 UT, in the
424 middle of a GC, indicate velocities around 0 m s^{-1} between cloud top and about 4.1 km
425 altitude, with the falling (negative velocities) particles clearly evident at lower altitudes.
426 The bi-modality around 3.8 km altitude (at the base of the GCs) suggests the presence
427 of a second SLW droplet population.

428 *3.3.3 SLW layers and precipitation phase*

429 Figure 16 shows the clouds and precipitation observed toward the end of the pas-
430 sage of the Case 3 cyclone. Although thick, low-level SLW cloud identified in the MPL

431 data before 10 UT mostly obscures the clouds at higher levels, we can see that SLW clouds
432 exist above 4km at temperatures as low as -31°C . There are two distinct high-altitude
433 SLW cloud layers just above, at 07 UT, separated vertically by about 500 m. The high-
434 est SLW layer does not appear to be precipitating. Likewise, a careful examination of
435 the low-level SLW clouds suggests that there are two SLW layers here.

436 After 11 UT, a precipitating SLW cloud layer persists for two hours at an altitude
437 of 4.2 km and cloud top temperature of -31°C . Retrievals from MODIS Aqua taken near
438 11 UT and MODIS Terra near 0530 UT on 16 February (MYD/MODIS products) both
439 indicate the region near the ship covered by primarily liquid phase clouds with a cloud-
440 top near 4 km, along with some smaller patches of ice cloud (not shown). Liquid par-
441 ticle effective radius was near or below $10\ \mu\text{m}$, with lower overall optical depths during
442 the overpass near 11 UT, all of which is consistent with the radar and lidar observations.
443 The δ_v (Figure 16c) indicates the predominance of ice precipitation beneath this mid-
444 level cloud. Streaks of ice from higher altitudes (visible in the MWACR data in Figure 16a)
445 intercept this SLW layer on occasion, which act to seed the SLW layer. These seeding
446 events may be a factor in the decay of the SLW layer. The radiosonde launched at 1130 UT
447 (Figure 17) passed through this virga and SLW layer: the stable top above the SLW layer
448 around 4.5 km altitude is clearly evident. The thermodynamic profiles below 0.5 km al-
449 titude again show the typical characteristics of the katabatic wind at Mawson (Vignon
450 et al., 2019). The well-mixed convective boundary layer tops out around 1.7 km, which
451 corresponds to cloud virga base. The liquid water path (LWP) is low during this event
452 and there is little, if any, evidence for supercooled drizzle.

453 **4 Discussion**

454 The synoptic structure differed for each of the three cases examined here, yet all
455 revealed the prevalence of MPCs. Extensive clouds observed during the transit into Davis
456 existed due to the presence of a weak trough, whereas observations made during the two
457 Mawson-based case studies encompassed both the warm and cold sectors of the cyclones.
458 For the two Mawson case studies, the cyclones decayed as they propagated eastward. All
459 events showed the typical three stages of cloud and precipitation observed in cloud sys-
460 tems along the East Antarctic coastline, specifically, (i) pre-precipitation virga falling
461 out of SLW layers at the start of the event, (ii) precipitation reaching the surface (char-
462 acterised by the strong radar reflectivities) during the event, and finally (iii) post-precipitation

463 virga in the trailing SLW layers. (Jullien et al., 2020), Multiple layers of SLW cloud were
464 embedded within ice clouds of large vertical extent (i. e. several kilometers deep) for sev-
465 eral hours during the central phase of each event (see Figure 3, Figure 9 and Figure 14).
466 This consistent cloud and virga/precipitation structure observed during all three events
467 suggests the ubiquitous occurrence of SLW layers within synoptic-scale cloud systems
468 in the high-latitude austral summer Southern Ocean.

469 However, small differences in precipitation phase, cloud seeding, and the altitude
470 of the trailing clouds were observed between events. The trailing clouds observed dur-
471 ing the events consisted of a single SLW layer in regions of very light wind speeds ($< 5 \text{ m s}^{-1}$)
472 either at the top of the boundary layer (Case 2) or as part of a mid-level MPC (Case 1
473 and Case 3). SLW cloud top temperatures during Case 3 were no warmer than -31°C .
474 In all three cases, ice precipitation from the single SLW layer continues for several hours.
475 Ice precipitation was enhanced during Case 2 and Case 3 at Mawson by higher-level seeder
476 ice clouds feeding the SLW layer (Figure 11 and Figure 16), similar to cloud seeding of
477 mid-level SLW layers reported in the tropics (Ansmann et al., 2009), northern mid-latitudes
478 (Herzogh & Hobbs, 1980; Hobbs et al., 1980) and the Arctic (Hobbs & Rangno, 1998).

479 Generating cells and their associated precipitating ice fall streaks have been exten-
480 sively documented for extra-tropical Northern Hemisphere cyclones; recent examples in-
481 clude Kumjian et al. (2014); Rosenow et al. (2014); Rauber et al. (2015); Keppas et al.
482 (2018). We summarise our findings for the generating cells observed adjacent to the Antarc-
483 tic in Table 2. GCs with similar physical characteristics to these Antarctic cases were
484 recently observed over the continental United States (Evans et al., 2005; Rosenow et al.,
485 2014) and the Arctic (McFarquhar et al., 2011). The mean horizontal extent of GCs re-
486 ported from aircraft observations over the open Southern Ocean is 0.4 km (Y. Wang et
487 al., 2020), lower than the cases adjacent to East Antarctica discussed here. This differ-
488 ence may be due to either a different environment close to the Antarctic (subject to mar-
489 time and continental influences), or the limited number of samples discussed here. Our
490 observations of a large range in temperatures of the GCs (-13°C to -30°C) is consis-
491 tent with the spread noted elsewhere (Evans et al., 2005; Kumjian et al., 2014).

492 The GCs reported directly offshore of Antarctica exist in mid-level clouds which
493 are topped by an SLW layer (which is either seen directly by the lidar, or inferred based
494 on large vertical motion and temperature inversion reported by radiosonde), and all ex-

495 hibited ice precipitation. Air-motion induced oscillations are evident in the GC regions
496 near cloud tops. A region of increasing negative (downward) Doppler velocity is present
497 beneath the GC turbulence region which is likely due to the growth of solid particles in
498 the more quiescent air. This particle growth could be due to riming, which increases the
499 mass to cross-sectional area ratio. Doppler velocities are maximum downward above 1.5 km
500 (the altitude of the lowest SLW layer) for the 26 January event offshore of Davis (Fig-
501 ure 6). The ice particles then sublimate in the very dry air below this lowest SLW layer
502 and Doppler velocities increase near the base of the cloud. This increase is likely due to
503 snow losing cross sectional area and becoming more spherical as the particles become
504 smaller, thereby increasing velocity even as the total condensed mass decreases. The widths
505 of the Doppler spectra near cloud base (or surface) are much larger for the two Maw-
506 son cases than the first case. The narrowness of the 26 January event suggests a nearly
507 mono-dispersive snow power spectral density (assuming little to no turbulence or mean
508 motion in the sub cloud region), while the two Mawson cases have much broader spec-
509 tra. In particular, the Doppler spectra for 1048 UT 15 February is very broad below 0.5 km
510 altitude (Figure 15c). The radiosonde profile from 1130 UT 15 February clearly indicates
511 a well-mixed katabatic layer at these low altitudes which is sufficiently turbulent to al-
512 ter the Doppler motion of the precipitating ice.

513 Observations of the multiple SLW layers during Case 1 (Figure 7) and coincident
514 radiosonde profile data indicate that the lowest SLW cloud layer is likely associated with
515 the convective boundary layer while the top SLW layer is likely due to turbulent updrafts.
516 Turbulence driven by cloud-top radiative cooling of the upper SLW layer, in which gen-
517 erating cells are evident (see Figure 6), is likely the main driver of the updrafts (Heymsfield
518 et al., 1991; Hogan et al., 2003), although the strong wind shear within the cloud will
519 also enhance mixing in this layer. In Case 1, a third (middle) SLW layer around 2.3 km
520 is apparent before 19 UT. All three cases featured such embedded (multiple) SLW lay-
521 ers, consistent with the idea that embedded SLW layers within deep ice clouds can be
522 driven by turbulent mixing, and will persist as long as turbulent processes continue (Field
523 et al., 2014). Multiple SLW layers can additionally be maintained via the longwave ra-
524 diative effect. Cloud-resolving modelling of Arctic multi-layer MPCs indicated that cloud
525 base radiative warming of the upper layer creates a gap in stability between two MPC
526 layers (Luo et al., 2008).

Precipitation out of the base of the SLW layers changed phase in two of the three case studies, in both cases near the end of the event. The supercooled drizzle persisted for about 2 hours in both cases, before changing to predominantly ice precipitation. The LWP during both precipitating drizzle episodes is $50 - 100 \text{ g m}^{-2}$. Non-precipitating SLW clouds in the mid-latitude Southern Ocean generally have $\text{LWP} < 50 \text{ g m}^{-2}$ (Mace & Protat, 2018b). The LWP in the present high-latitude Southern Ocean studies are large enough that drizzle is likely present during the periods identified in Section 3, while supercooled drizzle is either light or not likely present once the LWP dropped well below 50 g m^{-2} . The phase change from supercooled drizzle to ice precipitation was associated with seeding from higher clouds. Supercooled drizzle was present at temperatures between -15°C (cloud base) to -2°C (close to the surface) during these two events. Secondary ice multiplication processes will lead to an increase in ice crystal number concentration within these temperature ranges (Hallett & Mossop, 1974). Given the presence of supercooled drizzle in two out of the three cases presented here, it is likely that this is a common occurrence in cyclonic systems above the Southern Ocean and coastal Antarctic, including within the Hallett-Mossop zone. Supercooled drizzle-sized droplets potentially have important implications for secondary ice production processes over the high-latitude Southern Ocean (Young et al., 2018) as the freezing drizzle is suspected to eject many small droplets, favouring ice multiplication (Korolev et al., 2020).

5 Conclusions

Cloud remote-sensing instruments including W-band radar, a micropulse lidar and a microwave radiometer were mounted aboard an icebreaking vessel *RSV Aurora Australis* during austral summer 2017-18 as it transited the Southern Ocean. We characterise the fine-scale vertical structure and evolution of clouds and precipitation phase present in three systems which passed over the ship when it was between 64°S and 69°S , close or adjacent to the East Antarctic coast.

Multiple layers of SLW were embedded within ice clouds (with cloud tops of 2 – 6 km altitude). The trailing clouds observed in these systems were SLW-topped MPCs, which continued to precipitate ice, either at the top of the boundary layer or at mid-levels. This ice precipitation out of the SLW was enhanced in some cases by seeding from higher-level ice clouds. Ice precipitation is nearly continuous in all but the trailing SLW cloud layer(s) observed as the cyclonic systems are advected away from the ship.

559 Convective generating cells (GCs) were present within mid-level SLW-layer topped
560 MPCs and had physical scales (vertical extents up to 1.0 km and horizontal extent up
561 to 3.6 km) and upward Doppler motions ($0.5 - 1.0 \text{ m s}^{-1}$) consistent with observations
562 of GCs made previously at lower latitudes. Supercooled drizzle was observed during two
563 of the three events studied. In both cases the precipitation phase changed from drizzle
564 to predominantly ice following seeding of the drizzling SLW layer by a higher-level ice
565 cloud. The supercooled drizzle events both persisted for around 2 hours, and the driz-
566 zle was present in temperatures as cold as -15°C and as warm as -2°C .

567 Following this characterisation of the fine-scale structure of mixed-phase clouds and
568 precipitation within cyclones adjacent to the Antarctic, the next step is to simulate these
569 events in high-resolution models. Although it is likely that models will have difficulty
570 producing and maintaining SLW, we suspect that by appropriately tuning the microphys-
571 ical schemes using MARCUS observations, we will be able to more accurately reproduce
572 the clouds' vertical structure, evolution and phase partitioning (Vignon et al., 2021). Such
573 a path to model improvement of Southern Ocean clouds could be informed by recent anal-
574 yses of geostationary satellite imagery, which are capable of providing cloud macrophys-
575 ical properties and information on subcloud phase beneath supercooled liquid cloud tops
576 (e. g. Noh et al. (2019)).

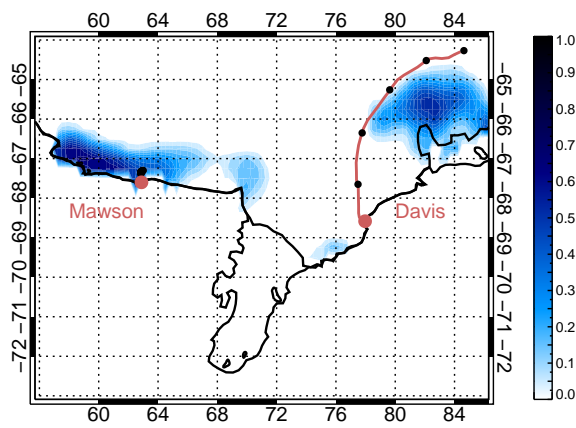


Figure 1. The East Antarctic region of interest. The red line indicates the passage southward into Davis of *RSV Aurora Australis* during Case 1, from 18 UT 25 January until 23 UT 26 January 2018. The small black filled circles indicate the locations of radiosonde launches during the three case studies. The blue contour scale indicates the mean sea ice concentration for February 2018, taken from ERA5 reanalysis.

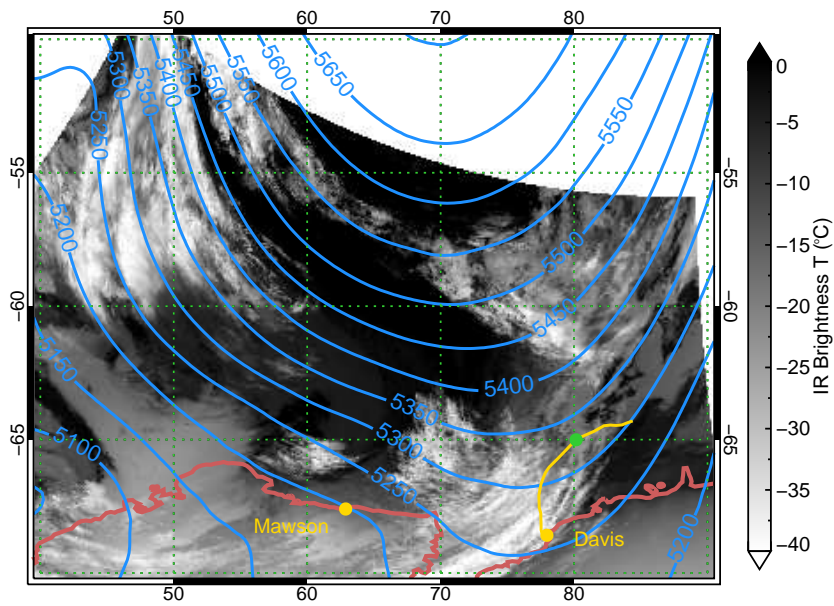


Figure 2. Infra-red brightness temperature (units $^{\circ}\text{C}$) for the METOP-A overpass at 04 UT 26 January, along with the ERA-5 500 hPa geopotential height at the same time (blue lines, units m). The yellow line indicates the passage southward into Davis of *RSV Aurora Australis* during Case 1, from 18 UT 25 January until 23 UT 26 January 2018, while the green filled circle indicates the ship's location at 04 UT 26 January. Mawson and Davis stations are indicated by the yellow filled circles

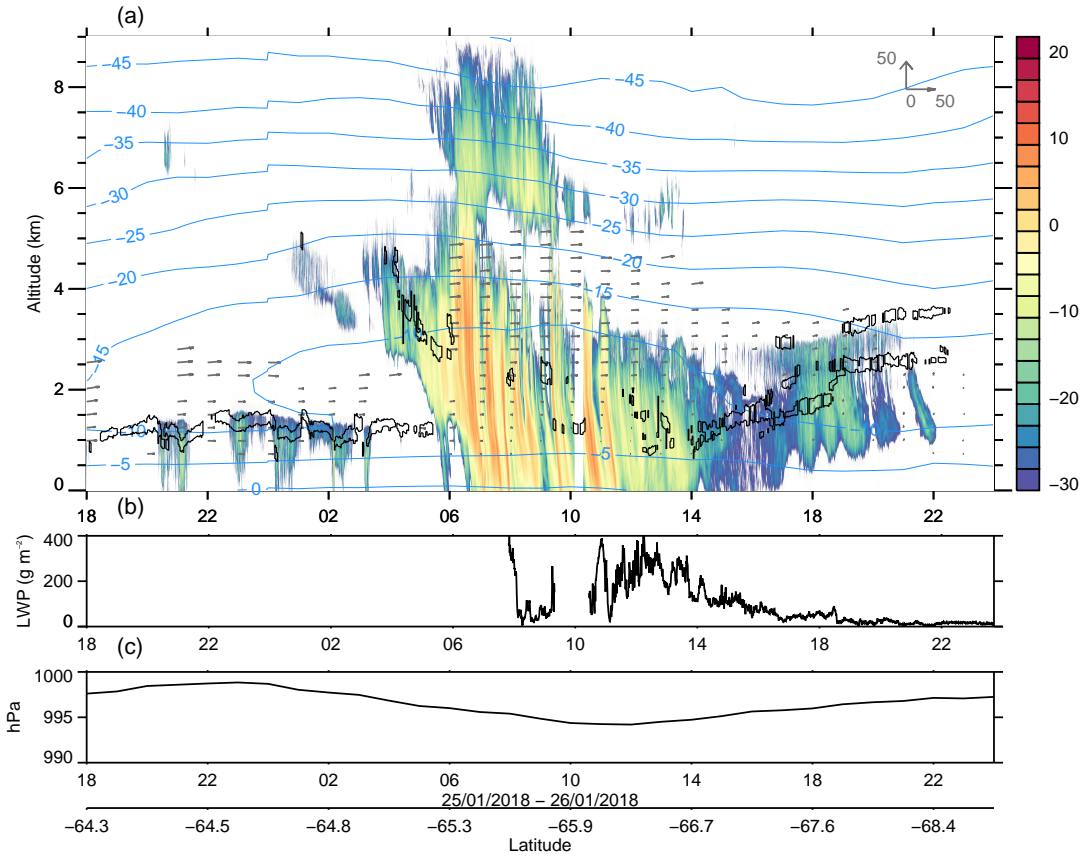


Figure 3. (a) Overview of cloud field and thermodynamic observations made during Case 1. The MWACR reflectivity is shown by the colour (units dBZ). The MPL data are used to determine the location of supercooled liquid water (SLW) clouds (black outlines). The ERA5 temperature field (blue, units of °C) is indicated. A subset of the BSRWP horizontal wind field (grey vectors) are displayed for clarity. Vectors of length 50 m s^{-1} are shown in the top right of panel (a), with the upward arrow indicating the northward direction and the rightward arrow indicating eastward. (b) Liquid water path derived from the MWR: these data were unavailable for the first half of this Case. (c) Surface pressure recorded onboard *RSV Aurora Australis*. The latitude of the observations is given at the bottom.

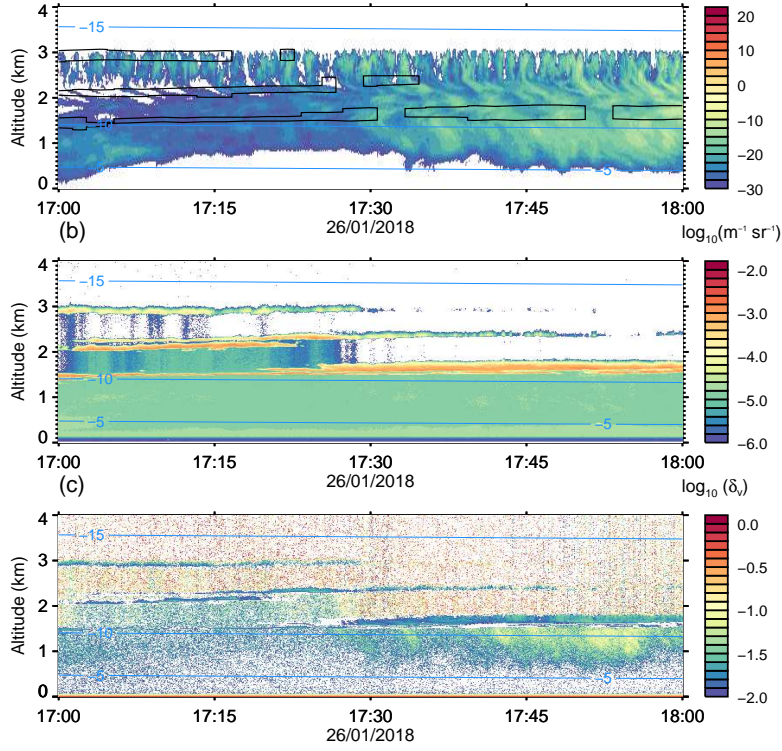


Figure 4. (a) Super-cooled liquid water clouds (black outline) and MWACR reflectivity (colour, units dBZ) between 17 – 18 UT 26 January 2018. (b) The MPL calibrated attenuated backscatter β_{att} and (c) the volume depolarisation ratio δ_v . ERA5 temperatures (units of $^{\circ}\text{C}$) are indicated by the blue lines on all panels.

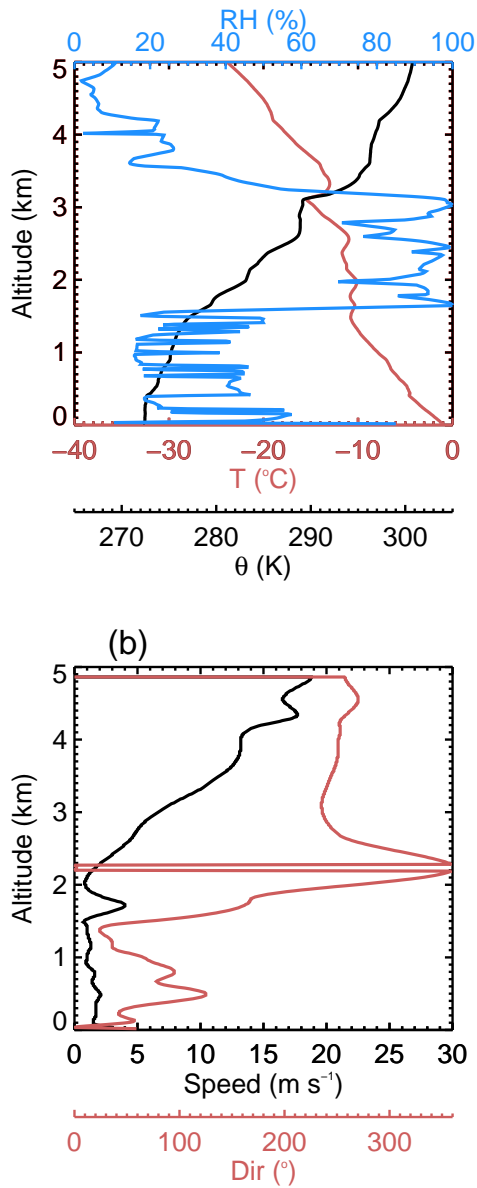


Figure 5. Radiosonde data from the 1732 UT launch on 26 January 2018. (a) Temperature (red), potential temperature (black) and relative humidity with respect to liquid (blue); (b) wind speed (black) and direction which the wind is from (red).

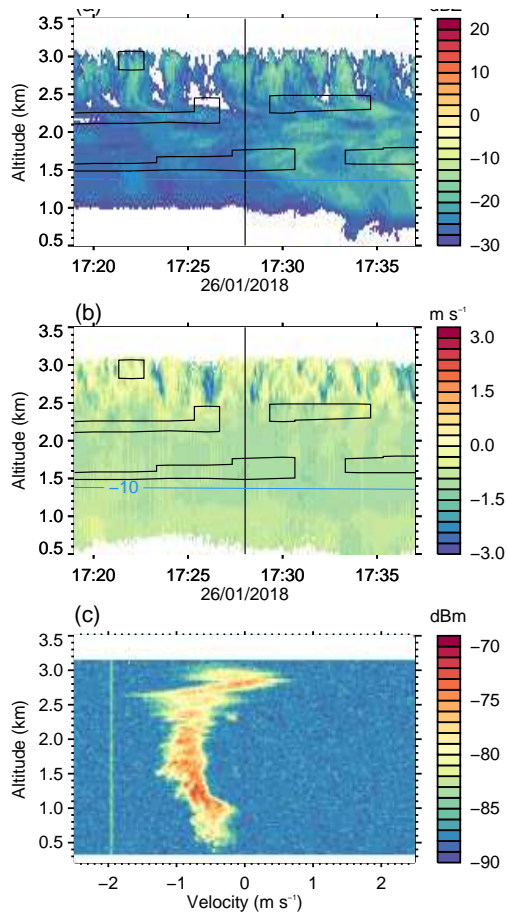


Figure 6. (a) MWACR reflectivity (dBZ) and (b) Doppler velocity (m s^{-1} , positive indicates upward motion) from 1719 - 1737 UT 26 January 2018. (c) The MWACR velocity spectra (dBm) at 1728 UT. The SLW clouds, calculated from two-minute MPL averaged data, are overlain as the black outlines in (a) and (b). The vertical line in (a) and (b) indicates the time of the spectra shown in (c). The ship's location was (67.6°S , 77.4°E) at this time.

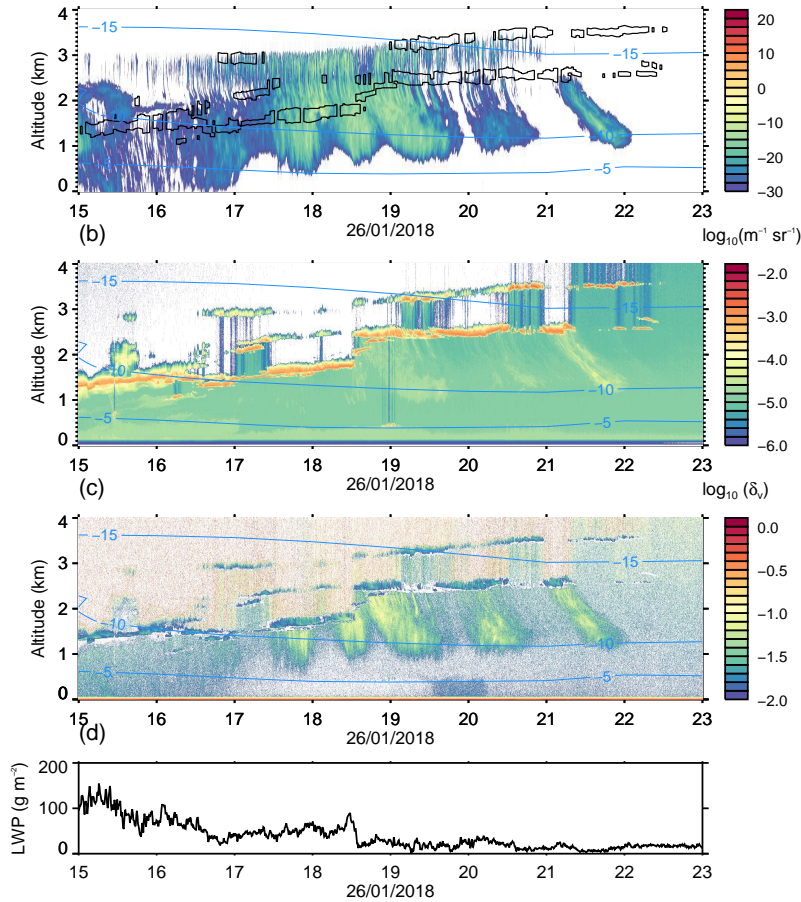


Figure 7. (a) MWACR reflectivity (colour contours, units dBZ) along with the SLW cloud extent determined from the MPL data (black outlines) on 26 January 2018. (b) The MPL calibrated attenuated backscatter β_{att} during the same interval. (c) The volume depolarisation ratio δ_v calculated from the MPL channels. ERA5 temperatures are indicated on all these panels (blue lines, units $^{\circ}\text{C}$) (d) Liquid water path derived from the MWR.

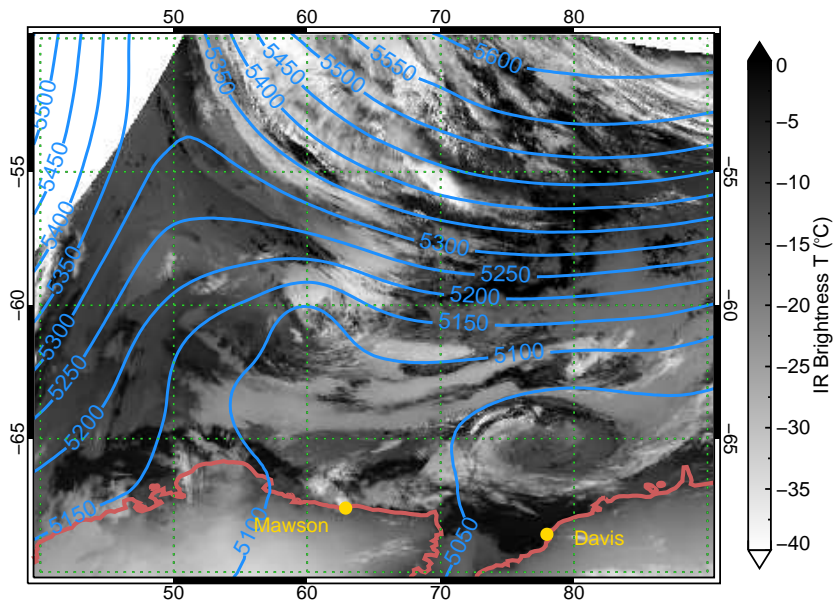


Figure 8. Infra-red brightness temperature (units $^{\circ}\text{C}$) for the METOP-B overpass at 04 UT 13 February, along with the ERA-5 500 hPa geopotential height at the same time (blue lines, units m). The ship is at Mawson station.

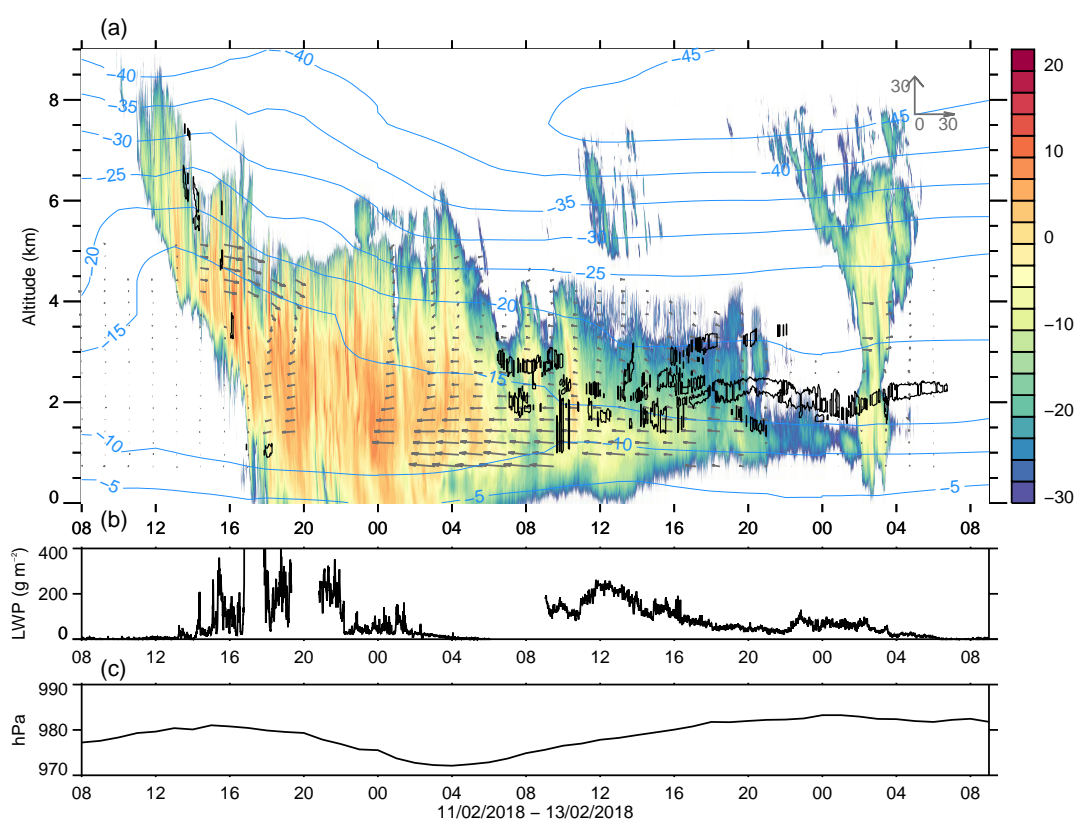


Figure 9. As for Figure 3 except showing the cloud and thermodynamic fields during Case 2, 11 – 13 February 2018, when the ship was at Mawson. Vectors of length 30 m s^{-1} are shown in the top right of panel (a), with the upward arrow indicating the northward direction and the rightward arrow indicating eastward. Data gaps in the MWR LWP and the BSRWP winds are evident.

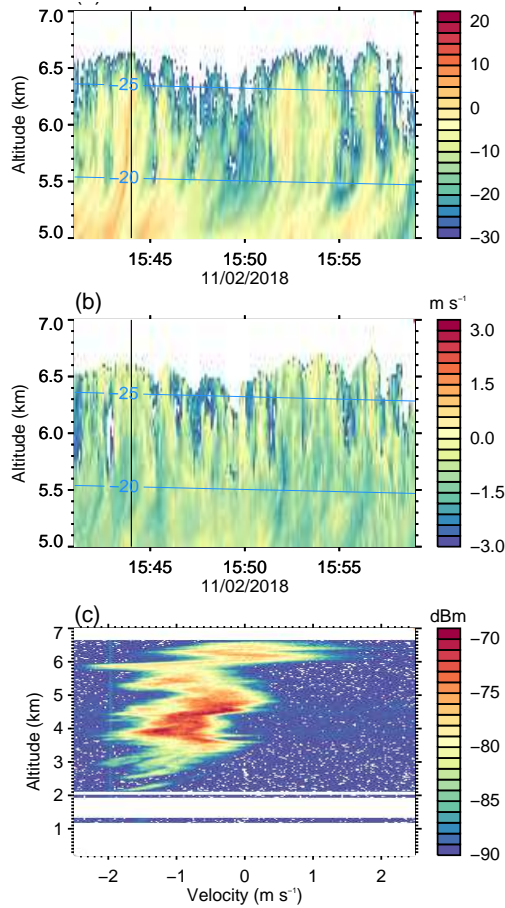


Figure 10. (a) MWACR reflectivity (dBZ) and (b) Doppler velocity (m s^{-1} , positive indicates upward motion) from 1541 – 1559 UT 11 February 2018. (c) The MWACR velocity spectra (dBm) at 1544 UT (note the different y -axis in this panel, from surface to cloud top). The vertical line in (a) and (b) indicates the time of the spectra shown in (c).

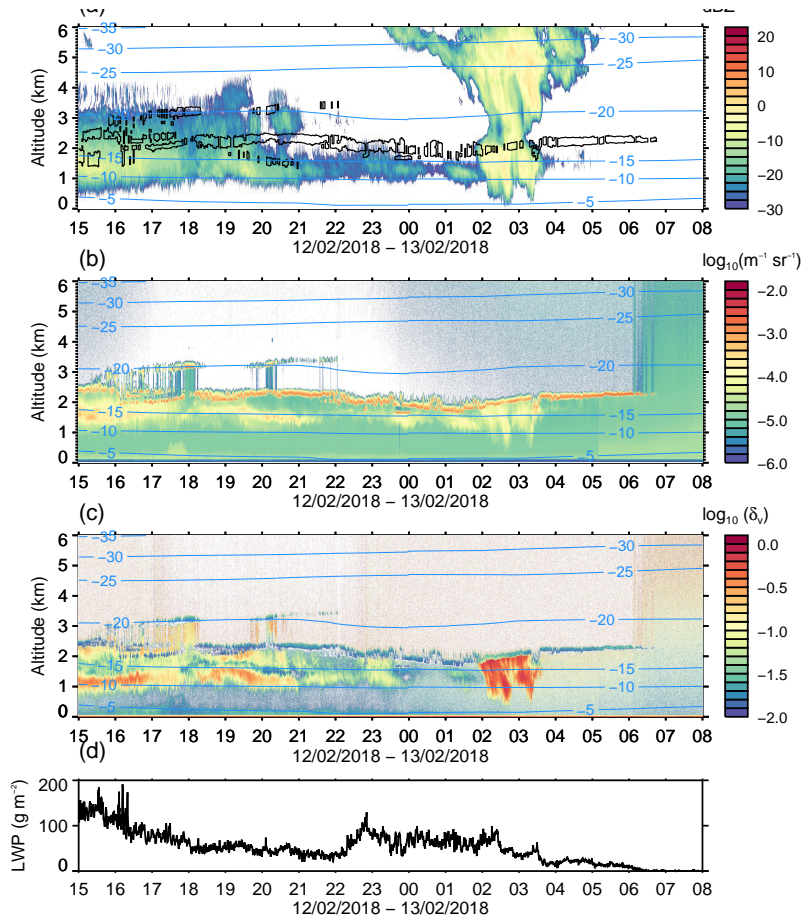


Figure 11. As for Figure 7, except showing the observations between 15 UT 12 February and 08 UT 13 February 2018.

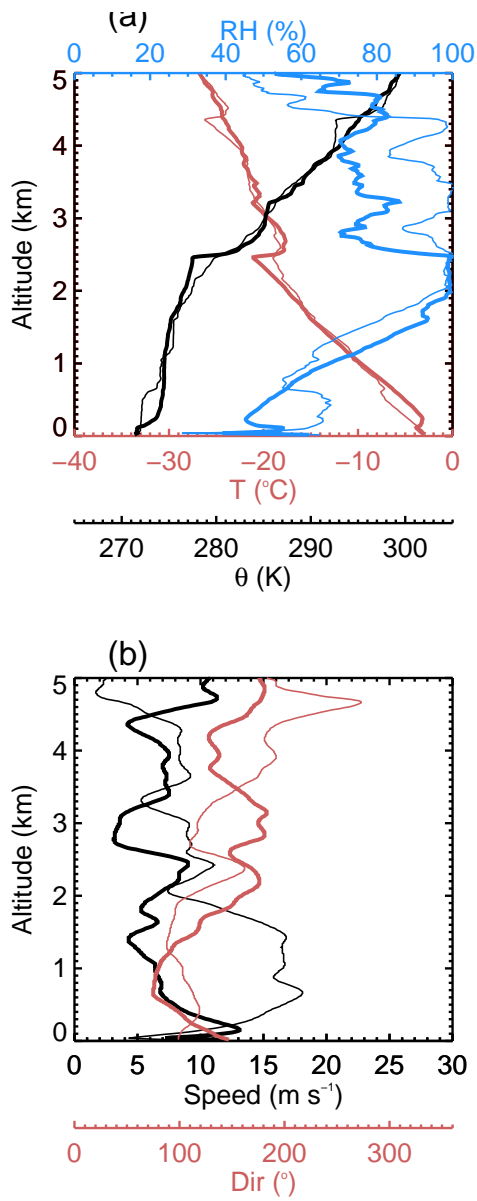


Figure 12. Radiosonde data from the 1730 UT (thin) and 2332 UT (thick) launches on 12 February 2018. (a) Temperature (red), potential temperature (black) and relative humidity with respect to liquid (blue); (b) wind speed (black) and direction which the wind is from (red).

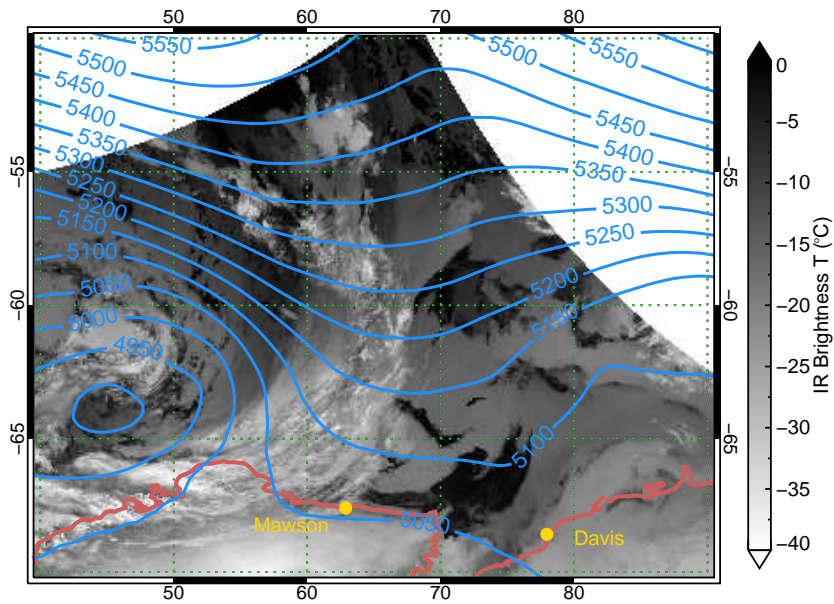


Figure 13. Infra-red brightness temperature (units °C) for the METOP-B overpass at 19 UT 14 February, along with the ERA-5 500 hPa geopotential height at the same time (blue lines, units m). The ship is at Mawson station

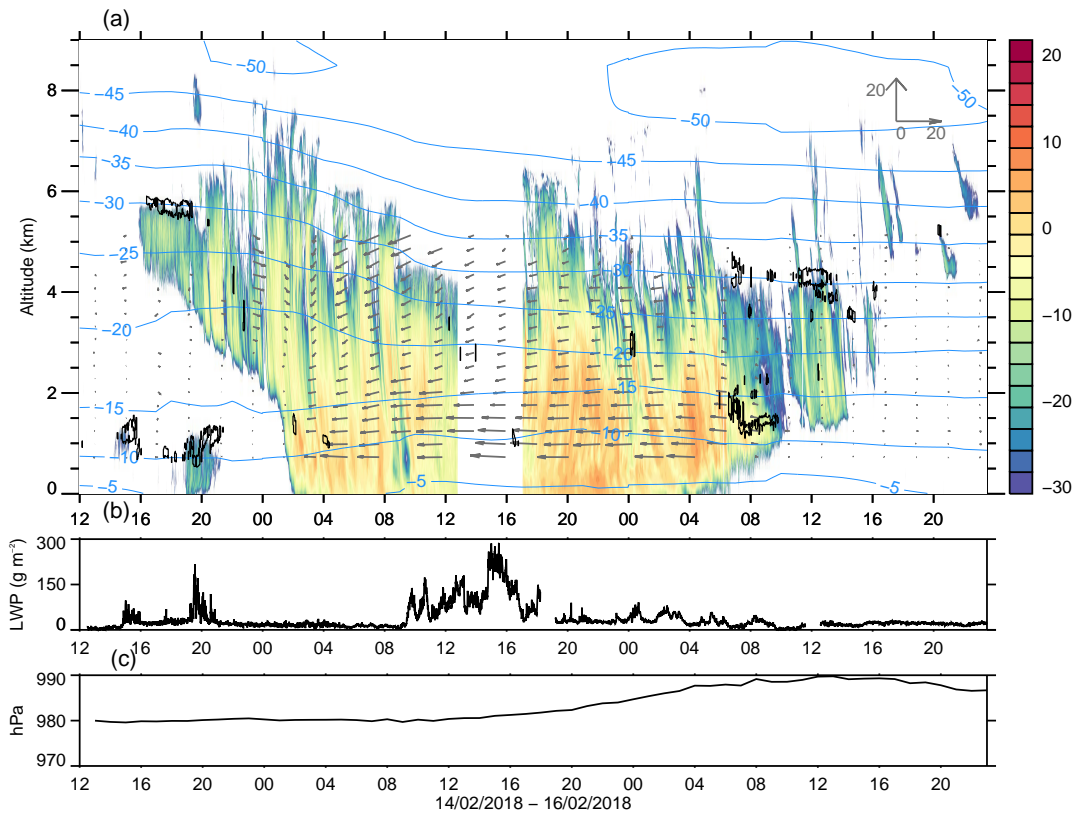


Figure 14. As for Figure 3 except showing the cloud and thermodynamic fields during Case 3, 14 – 16 February 2018, when the ship was at Mawson. Vectors of length 20 m s^{-1} are shown in the top right of panel (a), with the upward arrow indicating the northward direction and the rightward arrow indicating eastward. The MWACR cloud radar was not operational between 13 – 17 UT, 15 February.

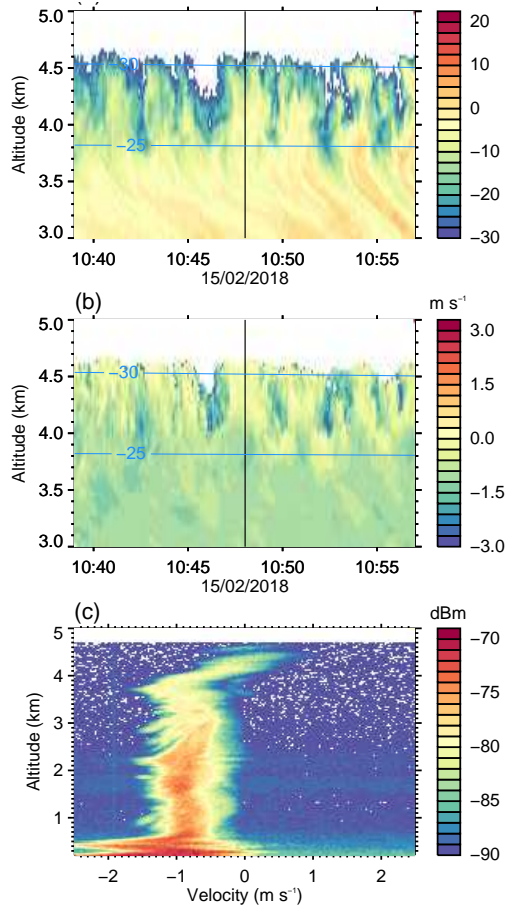


Figure 15. (a) MWACR reflectivity (dBZ) and (b) Doppler velocity (m s^{-1} , positive indicates upward motion) from 1039 – 1057 UT 15 February 2018. (c) The MWACR velocity spectra (dBm) at 1048 UT (note the different y -axis in this panel, from surface to cloud top). The vertical line in (a) and (b) indicates the time of the spectra shown in (c).

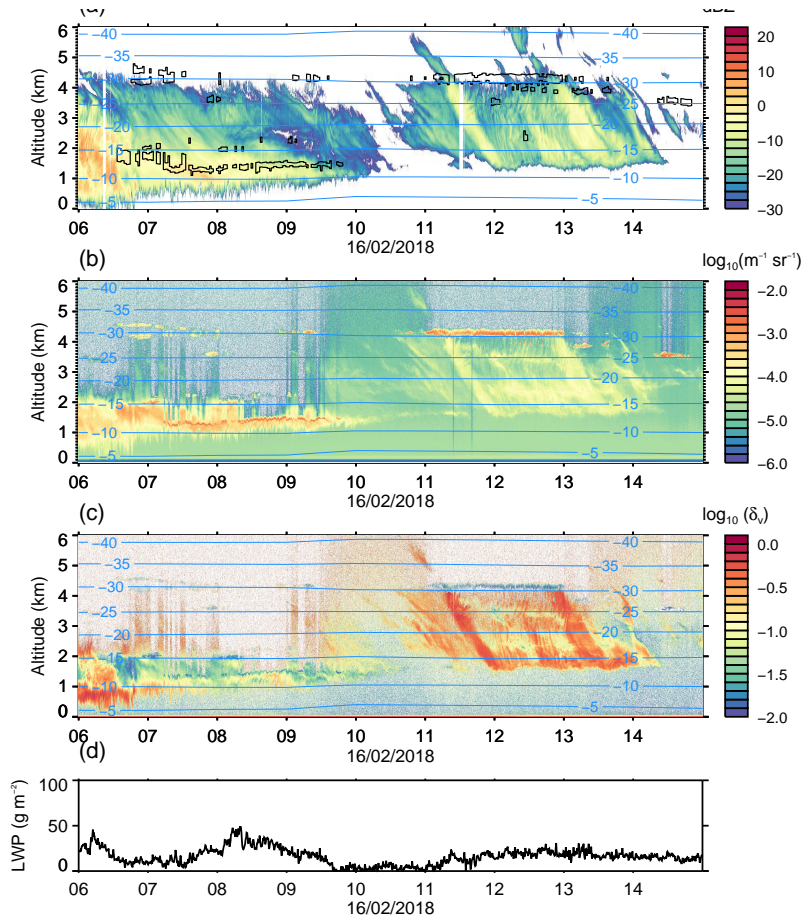


Figure 16. As for Figure 7, except showing the observations between 06 UT and 15 UT 16 February 2018.

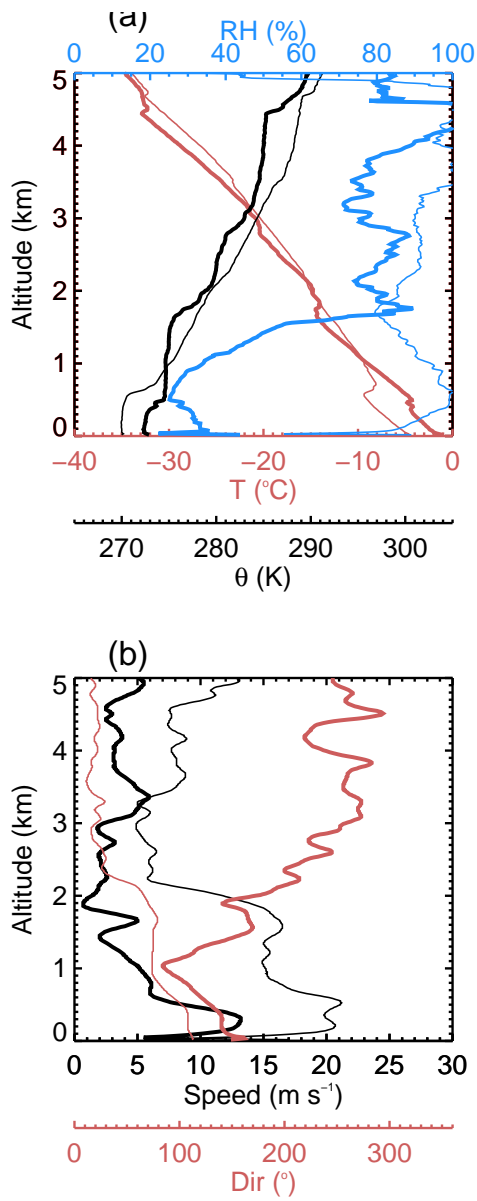


Figure 17. Radiosonde data from the 1130 UT 15 February (thin) and 1130 UT 16 February (thick) launches. (a) Temperature (red), potential temperature (black) and relative humidity with respect to liquid (blue); (b) wind speed (black) and direction which the wind is from (red).

Table 1. MARCUS instrumentation and their data used in the present study.

Instrument	Observed or derived parameters used
Marine W-band Cloud Radar (MWACR)	Reflectivity, Doppler velocity
Micro-pulse lidar (MPL)	Backscatter, depolarisation ratio, cloud extent, cloud phase
Radiosondes	Temperature, humidity, wind velocities
Backscatter radar wind profiler (BSRWP)	Horizontal wind velocities
2-channel microwave radiometer (MWR)	Liquid water path, precipitable water vapor

Table 2. Physical characteristics of generating cells observed adjacent to Antarctica. The temperature T , from ERA5, given below is that at cloud top height. Horizontal extent of the GCs are calculated using the radiosonde-derived wind speeds and directions, and the ship motion, as described in Section 3. The Doppler velocities given here are not corrected for the ship's negligible heave velocities (see text for details).

Case	Date	T	Horizontal extent	Vertical extent	Maximum upward Doppler velocity
1	26 January	-13°C	1.2 km	0.7 – 0.8 km	1.0 m s^{-1}
2	11 February	-26°C	2.4 – 3.6 km	1.0 km	1.0 m s^{-1}
3	15 February	-30°C	0.6 – 1.8 km	0.9 km	0.5 m s^{-1}

Acknowledgments

Technical, logistical, and ship support for MARCUS were provided by the Australian Antarctic Division through Australian Antarctic Science Projects 4292 and 4387, and we thank Steven Whiteside, Lloyd Symonds, Rick van den Enden, Peter de Vries, Chris Young and Chris Richards for their assistance. MARCUS data were obtained from the Atmospheric Radiation Measurement (ARM) Program sponsored by the U.S. Department of Energy, Office of Science, Office of Biological and Environmental Research, and Climate and Environmental Sciences Division. We thank all of the ARM technicians who collected the data and maintained the instruments onboard *RSV Aurora Australis*. ARM-MARCUS data used in this study may be downloaded from <https://adc.arm.gov/discovery/>, while ERA5 data are available at <https://cds.climate.copernicus.eu/>. METOP satellite images are available at <https://navigator.eumetsat.int/>. Ship surface meteorological and position data are available through the Australian Antarctic Data Centre <https://>

590 data.aad.gov.au. The MPL calibrated backscatter and derived cloud phase products,
591 along with the LWP and IWC from the MWR are permanently archived at [https://](https://data.aad.gov.au/metadata/records/AAS_4292_MARCUS_Case_Studies)
592 data.aad.gov.au/metadata/records/AAS_4292_MARCUS_Case_Studies (Alexander, 2020).
593 All data are freely available following registration. The contribution of GM was supported
594 by DoE BER award DE-SC0018626. The Bureau of Meteorology's contribution to this
595 study was partly funded by the National Environmental Science Program (NESP), Aus-
596 tralia, and the Australian Antarctic Program Partnership (AAPP). We thank two anony-
597 mous reviewers whose insightful comments helped improve an earlier version of this manuscript.

598 References

- 599 Alexander, S. P. (2020). *Derived data products produced from MARCUS cyclone ob-*
600 *servations, January-February, 2018.* Australian Antarctic Data Centre. (Ver-
601 sion 1, Last accessed: 2020-10-27) doi: 10.4225/15/58eedd2fd5a6b
- 602 Alexander, S. P., Klekociuk, A. R., McDonald, A. J., & Pitts, M. C. (2013). Quan-
603 tifying the role of orographic gravity waves on polar stratospheric cloud occur-
604 rence in the Antarctic and the Arctic. *J. Geophys. Res.*, *118*, 11,493–11,507.
605 doi: 10.1002/2013JD020122
- 606 Alexander, S. P., Orr, A., Webster, S., & Murphy, D. J. (2017). Observations
607 and fine-scale model simulations of gravity waves over Davis, East Antarctica
608 (69°S, 78°E). *J. Geophys. Res.*, *122*. doi: 10.1002/2017JD026615
- 609 Alexander, S. P., & Protat, A. (2018). Cloud properties observed from the surface
610 and by satellite at the northern edge of the Southern Ocean. *J. Geophys. Res.*,
611 *123*. doi: 10.1002/2017JD026552
- 612 Alexander, S. P., & Protat, A. (2019). Vertical profiling of aerosols with a com-
613 bined Raman-elastic backscatter lidar in the remote Southern Ocean marine
614 boundary layer (43°S - 66°S, 132°E - 150°E). *J. Geophys. Res.*, *124*. doi:
615 10.1029/2019JD030628
- 616 Ansmann, A., Tesche, M., Seifert, P., Althausen, D., Engelmann, R., Fruntke, J.,
617 ... Müller, D. (2009). Evolution of the ice phase in tropical altocumulus:
618 SAMUM lidar observations over Cape Verde. *J. Geophys. Res.*, *114*(D17208).
619 doi: 10.1029/2008JD011659
- 620 Barrett, P. A., Blyth, A., Brown, P. R. A., & Abel, S. J. (2020). The struc-
621 ture of turbulence and mixed-phase cloud microphysics in a highly su-

- 622 percooled altocumulus cloud. *Atmos. Chem. Phys.*, *20*, 1921–1939. doi:
623 10.5194/acp-20-1921-2020
- 624 Burrows, S. M., Hoose, C., Pöschl, U., & Lawrence, M. G. (2013). Ice nuclei in ma-
625 rine air: biogenic particles or dust? *Atmos. Chem. Phys.*, *13*, 245–267. doi: 10
626 .5194/acp-13-245-2013
- 627 Ceppi, P., Hartmann, D., & Webb, M. J. (2016). Mechanisms of the negative short-
628 wave cloud feedback in middle to high latitudes. *J. Climate*, *29*, 139–157. doi:
629 10.1175/JCLI-D-15-0327.1
- 630 Choi, Y. S., Ho, C. H., Park, C. E., Storelvmo, T., & Tan, I. (2014). Influence of
631 cloud phase composition on climate feedbacks. *J. Geophys. Res.*, *119*, 3687–
632 3700. doi: 10.1002/2013JD020582
- 633 Chubb, T. H., Jensen, J. B., Siems, S. T., & Manton, M. J. (2013). In situ ob-
634 servations of supercooled liquid clouds over the Southern Ocean during the
635 HIAPER Pole-to-Pole Observation (HIPPO) campaigns. *Geophys. Res. Lett.*,
636 *40*, 5280–5285. doi: 10.1002/grl.50986
- 637 Cunningham, J. G., & Yuter, S. E. (2014). Instability characteristics of
638 radar-derived mesoscale organization modes within cool-season precipi-
639 tation near Portland, Oregon. *Mon. Wea. Rev.*, *142*, 1738–1757. doi:
640 10.1175/MWR-D-13-00133.1
- 641 Evans, A. G., Locatelli, J. D., Stoelinga, M. T., & Hobbs, P. V. (2005). The
642 IMPROVE-1 storm of 12 February 2001. Part II: Cloud structures and the
643 growth of precipitation. *J. Atmos. Sci.*, *62*, 3456–3473. doi: 10.1175/
644 JAS3547.1
- 645 Field, P. R., Hill, A. A., K., F., & Korolev, A. (2014). Mixed-phase clouds in a
646 turbulent environment: Part 2: Analytic treatment. *Q. J. R. Meteorol. Soc.*,
647 *140*, 870–880. doi: 10.1256/qj.03.102
- 648 Field, P. R., Hogan, R. J., Brown, P. R. A., Illingworth, A. J., Choulaton, T. W.,
649 Kaye, P. H., . . . Greenaway, R. (2004). Simultaneous radar and aircraft obser-
650 vations of mixed-phase cloud at the 100 m scale. *Q. J. R. Meteorol. Soc.*, *130*,
651 1877–1904. doi: 10.1256/qj.03.102
- 652 Forbes, R. M., & Ahlgrim, M. (2014). On the representation of high-latitude
653 boundary layer mixed-phase cloud in the ECMWF global model. *Mon. Wea.*
654 *Rev.*, *142*, 3425–3445. doi: 10.1175/MWR-D-13-00325.1

- 655 Forbes, R. M., & Hogan, R. J. (2006). Observations of the depth of ice particle a-
656 vapouration beneath frontal cloud to improve NWP modelling. *Q. J. R. Meteorol.*
657 *Soc.*, *132*, 865–883. doi: 10.1256/qj.04.187
- 658 Gilbert, E., Orr, A., King, J. C., Renfrew, I. A., Lachlan-Cope, T., Field, P. F., &
659 Boutle, I. A. (2020). Summertime cloud phase strongly influences surface
660 melting on the Larsen C ice shelf, Antarctica. *Q. J. R. Meteorol. Soc.*, *146*,
661 1575–1589. doi: 10.1002/qj.3753
- 662 Hallett, J., & Mossop, S. C. (1974). Production of secondary ice particles during the
663 riming process. *Nature*, *249*, 26–28.
- 664 Haynes, J. M., Jakob, C., Rossow, W. B., Tselioudis, G., & Brown, J. (2011). Major
665 characteristics of southern ocean cloud regimes and their effects on the energy
666 budget. *J. Climate*, *24*, 5061–5080. doi: 10.1175/2011jcli4052.1
- 667 Hersbach, H., et al. (2020). The ERA5 Global Reanalysis. *Q. J. R. Meteorol. Soc.*,
668 *146*, 1999–2049. doi: 10.1002/qj.3803
- 669 Herzegh, P. H., & Hobbs, P. V. (1980). The mesoscale and microscale structure
670 and organisation of clouds and precipitation in midlatitude cyclones. II: Warm
671 frontal clouds. *J. Atmos. Sci.*, *37*, 597–611.
- 672 Heymsfield, A. J., Miloshevich, L. M., Slingo, A., Sassen, K., & Starr, D. O. (1991).
673 An observational and theoretical study of highly supercooled altocumulus. *J.*
674 *Atmos. Sci.*, *48*, 923–945.
- 675 Hobbs, P. V., Matejka, T. J., Herzegh, P. H., Locatelli, J. D., & Houze Jr, . R. A.
676 (1980). The mesoscale and microscale structure and organisation of clouds and
677 precipitation in midlatitude cyclones. I: A case study of a cold front. *J. Atmos.*
678 *Sci.*, *37*, 568–596.
- 679 Hobbs, P. V., & Rangno, A. L. (1998). Microstructures of low and middle-level
680 clouds over the Beaufort Sea. *Q. J. R. Meteorol. Soc.*, *124*, 2035–2071.
- 681 Hogan, R. J., Francis, P. N., Flentje, H., Illingworth, A. J., Quante, M., & Pelon, J.
682 (2003). Characteristics of mixed-phase clouds: Part i. Lidar, radar and aircraft
683 observations from CLARE98. *Q. J. R. Meteorol. Soc.*, *129*, 2089–2116.
- 684 Hu, Y., Rodier, S., Xu, K., Sun, W., Huang, J., Lin, B., . . . Josset, D. (2010).
685 Occurrence, liquid water content and fraction of supercooled water clouds
686 from combined CALIOP/IIR/MODIS measurements. *J. Geophys. Res.*,
687 *115*(D00H34). doi: 10.1029/2009JD012384

- 688 Huang, Y., Franklin, C. N., Siems, S. T., Manton, M. J., Chubb, T., Lock, A., ...
689 Klekociuk, A. R. (2015). Evaluation of boundary-layer cloud forecasts over the
690 Southern Ocean in a limited-area numerical weather prediction system using
691 in-situ, space-borne and ground-based observations. *Q. J. R. Meteorol. Soc.*,
692 *141*, 2259–2276. doi: 10.1002/qj.2519
- 693 Huang, Y., Siems, S. T., Manton, M. J., Protat, A., & Delanoë, J. (2012). A study
694 on the low-altitude clouds over the Southern Ocean using the DARDAR-
695 MASK. *J. Geophys. Res.*, *117*(D18204). doi: 10.1029/2012JD017800
- 696 Huang, Y., Siems, S. T., Manton, M. J., & Thompson, G. (2014). An evaluation
697 of WRF simulations of clouds over the Southern Ocean with ATrain observa-
698 tions. *Mon. Wea. Rev.*, *142*, 647–667. doi: 10.1175/MWR-D-13-00128.1
- 699 Jackson, R. C., McFarquhar, G. M., Korolev, A. V., Earle, M. E., Liu, P. S. K.,
700 Lawson, R. P., ... Freer, M. (2012). The dependence of ice microphysics on
701 aerosol concentration in Arctic mixed-phase stratus clouds during ISDAC and
702 M-PACE. *J. Geophys. Res.*, *117*(D15207). doi: 10.1029/2012JD017668
- 703 Jullien, N., Vignon, E., Sprenger, M., Aemisegger, F., & Berne, A. (2020). Synop-
704 tic conditions and atmospheric moisture pathways associated with virga and
705 precipitation over coastal Adélie Land in Antarctica. *The Cryosphere*, *14*,
706 1685–1702. doi: 10.5194/tc-14-1685-2020
- 707 Kanitz, T., Seifert, P., Ansmann, A., Engelmann, R., Althausen, D., Casiccia, C.,
708 & Rohwer, E. G. (2011). Contrasting the impact of aerosols at northern and
709 southern midlatitudes on heterogeneous ice formation. *Geophys. Res. Lett.*, *38*.
710 doi: 10.1029/2011GL048532
- 711 Kay, J. E., Wall, C., Yettella, V., Medeiros, B., Hannay, C., Caldwell, P., & Bitz,
712 C. (2016). Global climate impacts of fixing the Southern Ocean shortwave
713 radiation bias in the Community Earth System Model (CESM). *J. Climate*,
714 *29*, 46174636. doi: 10.1175/JCLI-D-15-0358.1
- 715 Keppas, S. C., Crosier, J., Choulaton, T. W., & Bower, K. N. (2018). Microphysi-
716 cal properties and radar polarimetric features within a warm front. *Mon. Wea.*
717 *Rev.*, *146*, 2003–2022. doi: 10.1175/MWR-D-18-0056.1
- 718 King, J. C., et al. (2015). Validation of the summertime surface energy budget of
719 Larsen C Ice Shelf (Antarctica) as represented in three high-resolution atmo-
720 spheric models. *J. Geophys. Res.*, *120*, 13351347. doi: 10.1002/2014JD022604

- 721 Klekociuk, A. R., French, W. J. R., Alexander, S. P., Kuma, P., & McDonald,
722 A. J. (2020). The state of the atmosphere in the 2016 southern Ker-
723 guelen Axis campaign region. *Deep Sea Research II*, *174*(104550). doi:
724 10.1016/j.dsr2.2019.02.001
- 725 Kollias, P., Treserras, B. P., & Protat, A. (2019). Calibration of the 2007
726 – 2017 record of Atmospheric Radiation Measurements cloud radar ob-
727 servations using CloudSat. *Atmos. Meas. Tech.*, *12*, 4949–4964. doi:
728 10.5194/amt-12-4949-2019
- 729 Korolev, A., Heckman, I., Wolde, M., Ackerman, A. S., Fridlind, A. M., Ladino,
730 L. A., ... Williams, E. (2020). A new look at the environmental conditions
731 favourable to secondary ice production. *Atmos. Chem. Phys.*, *20*, 1391–1429.
732 doi: 10.5194/acp-20-1391-2020
- 733 Korolov, A., & Field, P. R. (2008). The effect of dynamics on mixed-phase
734 clouds: Theoretical considerations. *J. Atmos. Sci.*, *65*, 66–86. doi:
735 10.1175/2007JAS2355.1
- 736 Kuma, P., et al. (2020). Evaluation of Southern Ocean cloud in the HadGEM3 gen-
737 eral circulation model and MERRA-2 reanalysis using ship-based observations.
738 *Atmos. Chem. Phys.*, *20*, 6607–6630. doi: 10.5194/acp-20-6607-2020
- 739 Kumjian, M. R., Rutledge, S. A., Rasmussen, R. M., Kennedy, P. C., & Dixon,
740 M. (2014). High-resolution polarimetric radar observations of snow-
741 generating cells. *J. Appl. Meteorol. Clim.*, *53*, 1636–1658. doi: 10.1175/
742 JAMC-D-13-0312.1
- 743 Lenaerts, J. T. M., Van Tricht, K., Lhermitte, S., & L'Ecuyer, T. S. (2017). Polar
744 clouds and radiation in satellite observations, reanalyses and climate models.
745 *Geophys. Res. Lett.*, *44*, 3355–3364. doi: 10.1002/2016GL072242
- 746 Listowski, C., Delanoë, J., Kirchgaessner, A., Lachlan-Cope, T., & King, J. (2019).
747 Antarctic clouds, supercooled liquid water and mixed-phase investigated with
748 DARDAR: geographical and seasonal variations. *Atmos. Chem. Phys.*, *19*,
749 67716808. doi: 10.5194/acp-2018-1222
- 750 Luo, Y., Xu, K.-M., Morrison, H., McFarquhar, G. M., Wang, Z., & Zhang, G.
751 (2008). Multi-layer arctic mixed-phase clouds simulated by a cloud-resolving
752 model: Comparison with ARM observations and sensitivity experiments. *J.*
753 *Geophys. Res.*, *113*(D12208). doi: 10.1029/2007JD009563

- 754 Mace, G. G. (2010). Cloud properties and radiative forcing over the maritime storm
755 tracks for the Southern Ocean and North Atlantic derived from A-Train. *J.*
756 *Geophys. Res.*, *115*(D10201). doi: 10.1029/2009JD012517
- 757 Mace, G. G., & Protat, A. (2018a). Clouds over the Southern Ocean as observed
758 from the R/V Investigator during CAPRICORN. Part I: Cloud occurrence
759 and phase partitioning. *J. Appl. Meteorol. Clim.*, *57*, 1783–1803. doi:
760 10.1175/JAMC-D-17-0194.1
- 761 Mace, G. G., & Protat, A. (2018b). Clouds over the Southern Ocean as observed
762 from the R/V Investigator during CAPRICORN. Part II: The properties of
763 non-precipitating stratocumulus. *J. Appl. Meteorol. Clim.*, *57*, 1805—1823.
764 doi: 10.1175/JAMC-D-17-0195.1
- 765 Mace, G. G., Protat, A., Humphries, R. S., Alexander, S. P., McRobert, I. M.,
766 Ward, J., ... Keyword, M. (2021). Southern Ocean cloud properties de-
767 rived from CAPRICORN and MARCUS data. *J. Geophys. Res.* doi:
768 10.1029/2020JD033368
- 769 Marchand, R., Ackerman, T., Smyth, M., & Rossow, W. B. (2009). A review
770 of cloud top height and optical depth histograms from MISR, ISCCP, and
771 MODIS. *J. Geophys. Res.*, *115*. doi: 10.1029/2009JD013422
- 772 Marchand, R., Ackerman, T., Westwater, E. R., Clough, S. A., Cady-Pereira, K., &
773 Liljegren, J. C. (2003). An assessment of microwave absorption models and re-
774 trievals of cloud liquid water using clear-sky data. *J. Geophys. Res.*, *108*(D24),
775 4773. doi: 10.1029/2003JD003843
- 776 McCluskey, et al. (2018). Observations of ice nucleating particles over South-
777 ern Ocean waters. *Geophys. Res. Lett.*, *45*, 11,98911,997. doi: 10.1029/
778 2018GL079981
- 779 McCoy, D. T., Hartmann, D. L., & Grosvenor, D. P. (2014). Observed south-
780 ern ocean cloud properties and shortwave reflection. Part I: Calculation of
781 SW flux from observed cloud properties. *J. Climate*, *27*, 8836–8857. doi:
782 0.1175/JCLI-D-14-00287.1
- 783 McFarquhar, G. M., et al. (2011). Indirect and semi-direct aerosol campaign: The
784 impact of Arctic aerosols on clouds. *Bull. Amer. Meteor. Soc.*, *144*(92), 183–
785 201. doi: 10.1175/2010BAMS2935.1
- 786 McFarquhar, G. M., et al. (2021). Observations of clouds, aerosols, precipita-

- 787 tion and surface radiation over the Southern Ocean: An overview of CAPRI-
788 CORN, MARCUS, MICRE and SOCRATES. *Bull. Amer. Meteor. Soc.*. doi:
789 10.1175/BAMS-D-20-0132.1
- 790 McFarquhar, G. M., Zhang, G., Poellot, M. R., Kok, G. L., McCoy, R., Tooman, T.,
791 ... Heymsfield, A. J. (2007). Ice properties of single-layer stratocumulus dur-
792 ing the Mixed-Phase Arctic Cloud Experiment: 1. Observations. *J. Geophys.*
793 *Res.*, *112*(D24201). doi: 10.1029/2007JD008633
- 794 Mioche, G., Jourdan, O., Ceccaldi, M., & Delanoë, J. (2015). Variability of mixed-
795 phase clouds in the Arctic with a focus on the Svalbard region: a study based
796 on spaceborne active remote sensing. *Atmos. Chem. Phys.*(15), 2445–2461. doi:
797 10.5194/acp-15-2445-2015
- 798 Morrison, A. E., Siems, S. T., & Manton, M. J. (2011). A three year climatology
799 of cloudtop phase over the Southern Ocean and North Pacific. *J. Climate*, *24*,
800 2405–2418. doi: 10.1175/2010JCLI3842.1
- 801 Morrison, H., de Boer, G., Feingold, G., Harrington, J., Shupe, M. D., & Sulia, K.
802 (2012). Resilience of persistent Arctic mixed-phase clouds. *Nature Geo.*, *5*,
803 11–17. doi: 10.1038/NGEO1332
- 804 Noh, Y.-J., Miller, S. D., Heidinger, A. K., Mace, G., Protat, A., & Alexander, S. P.
805 (2019). Satellite based detection of daytime supercooled liquidtopped mixed-
806 phase clouds over the Southern Ocean using the Advanced Himawari Imager.
807 *J. Geophys. Res.*, *124*. doi: 10.1029/2018JD029524
- 808 Orr, A., Phillips, R., Webster, S., Elvidge, A., Weeks, M., Hosking, J. S., & Turner,
809 J. (2014). Met Office Unified Model high resolution simulations of a strong
810 wind event in Antarctica. *Q. J. R. Meteorol. Soc.*. doi: 10.1002/qj.2296
- 811 Plummer, D. M., McFarquhar, G. M., Rauber, R. M., Jewett, B. F., & Leon, D. C.
812 (2015). Microphysical properties of convectively generated fall streaks within
813 the stratiform comma head region of continental winter cyclones. *J. Atmos.*
814 *Sci.*, *72*, 2465–2483. doi: 10.1175/JAS-D-14-0354.1
- 815 Protat, A., Schulz, E., Rikus, L., Sun, Z., Xiao, Y., & Keywood, M. (2017). Ship-
816 borne observations of the radiative effect of Southern Ocean clouds. *J. Geo-*
817 *phys. Res.*, *121*, 318328. doi: 10.1002/2016JD026061
- 818 Rauber, R. M., Plummer, D. M., Macomber, M. K., Rosenow, A. A., McFar-
819 quhar, G. M., & Jewett, B. F. (2015). The role of cloud-top generating

- 820 cells and boundary layer circulations in the finescale radar structure of a win-
821 ter cyclone over the Great Lakes. *Mon. Wea. Rev.*, *143*, 2291–2318. doi:
822 10.1175/MWR-D-14-00350.1
- 823 Rauber, R. M., & Tokay, A. (1991). An explanation for the existence of supercooled
824 water at the top of cold clouds. *J. Atmos. Sci.*, *48*, 1005–1023.
- 825 Rosenow, A. A., Plummer, D. M., Rauber, R. M., McFarquhar, G. M., Jewett,
826 B. F., & Leon, D. (2014). Vertical velocity and physical structure of generating
827 cells and convection in the comma head region of continental winter cyclones.
828 *J. Atmos. Sci.*, *71*, 15381558. doi: 10.1175/JASD130249.1
- 829 Sato, K., Inoue, J., Alexander, S. P., McFarquhar, G., & Yamazaki, A. (2018).
830 Improved reanalysis and prediction of atmospheric fields over the Southern
831 Ocean using campaign-based radiosonde observations. *Geophys. Res. Lett.*, *45*,
832 11,406–11,413. doi: 10.1029/2018GL079037
- 833 Sotiropoulou, G., Sedlar, J., Forbes, R., & Tjernström. (2016). Summer Arctic
834 clouds in the ECMWF forecast model: and evaluation of cloud parameterisa-
835 tion schemes. *Q. J. R. Meteorol. Soc.*, *142*, 387–400. doi: 10.1002/qj.2658
- 836 Storelvmo, T., Tan, I., & Korolev, A. (2015). Cloud phase changes induced by
837 CO₂ warming—a powerful yet poorly constrained cloud-climate feedback. *Curr.*
838 *Clim. Change Rep.*, *1*, 1–9. doi: 10.1007/s40641-015-0026-2
- 839 Tan, I., Storelvmo, T., & Zelinka, M. D. (2016). Observational constraints on mixed-
840 phase clouds imply higher climate sensitivity. *Science*, *352*, 224–227. doi: 10
841 .1126/science.aad5300
- 842 Turner, J., Chenoli, S. N., Samah, A. A., Marshall, G., Phillips, T., & Orr, A.
843 (2009). Strong wind events in the Antarctic. *J. Geophys. Res.*, *114*. doi:
844 10.1029/2008JD011642
- 845 Verlinde, J., Rambukkange, M. P., Clothiaux, E. E., McFarquhar, G. M., & Elo-
846 ranta, E. W. (2013). Arctic multilayered, mixed-phase cloud processes revealed
847 in millimeter-wave cloud radar Doppler spectra. *J. Geophys. Res.*, *118*, 13199–
848 13213. doi: 10.1002/2013JD020183
- 849 Vignon, E., Alexander, S. P., DeMott, P. J., Sotiropoulou, G., Gerber, F., Hill,
850 T. C. J., ... Berne, A. (2021). Challenging and improving the simulation
851 of mid-level mixed-phase clouds over the high-latitude Southern Ocean. *J.*
852 *Geophys. Res.*. (in review) doi: 10.1002/essoar.10503669.1

- 853 Vignon, E., Traullé, O., & Berne, A. (2019). On the fine vertical structure of the low
854 troposphere over the coastal margins of East Antarctica. *Atmos. Chem. Phys.*,
855 *19*, 46594683. doi: 10.5194/acp-19-4659-2019
- 856 Wang, Y., et al. (2020). Microphysical properties of generating cells over the South-
857 ern Ocean: Results from SOCRATES. *J. Geophys. Res.*, *125*. doi: 10.1029/
858 2019JD032237
- 859 Wang, Z., & Sassen, K. (2001). Cloud type and macrophysical property retrieval us-
860 ing multiple remote sensors. *J. Appl. Meteor.*, *40*, 1665–1682.
- 861 Young, G., Lachlan-Cope, T., O’Shea, S. J., Dearden, C., Listowski, C., Bower,
862 K. N., ... Gallagher, M. W. (2018). Radiative effects of secondary ice en-
863 hancement in coastal Antarctic clouds. *Geophys. Res. Lett.*, *46*, 2312–2321.
864 doi: 10.1029/2018GL080551